Study of Blade/Vortex interaction using Computational Fluid Dynamics and Computational Aeroacoustics

R. Morvant, K. J. Badcock, G. N. Barakos, and B. E. Richards

Computational Fluid Dynamics Lab,

Department of Aerospace Engineering,

University of Glasgow,

Scotland G12 8QQ, United Kingdom.

Abstract

A parametric study of the aerodynamics and the acoustics of parallel BVI has been carried out for different aerofoil shapes and vortex properties. Computing BVI using Computational Fluid Dynamics is challenging since the solution scheme tends to alter the characteristics of the vortex which must be preserved until the interaction. The present work uses the Compressible Vorticity Confinement Method (CVCM) for capturing the vortex characteristics, which is easier to implement and has minimal overhead in the performance of existing CFD solvers either in terms of CPU time or robustness during convergence. Apart from applying the CVCM method with an upwind solver, something not encountered in the literature, the present work couples CFD with Computational Aeroacoustics (CAA) and uses the strengths of both techniques in order to predict the nearfield and farfield noise. Results illustrate the importance of the aerofoil shape at transonic flow and show that the magnitude of the BVI noise depends strongly on the vortex strength and the miss-distance. The effect of the vortex core radius was also found to be important.

Notation

ε	Confinement parameter
$\hat{\Gamma}$	Normalised circulation
μ	Numerical viscosity, advance ratio
ω	Vorticity
ρ	Density
Σ	Surface
S	Source term
ϑ	Volume
$\vec{f}_b$	Body force term
$\vec{n}$	Normalised vorticity gradient vector to the surface S
$\vec{V}$	Velocity vector
M_{tip}	Tip Mach number
R	Rotor radius
r	Distance from the vortex core, radial co-ordinates
R_c	Non-dimensionalised core radius
U_∞	Freestream velocity
v_θ	Tangential velocity
y_0	Miss-distance
a	Speed of the sound
BVI	Blade Vortex Interaction
c	Chord length
CAA	Computational Aeroacoustics
CFD	Computational Fluid Dynamics
Cp	Surface pressure coefficient
CVCM	Compressible Vorticity Confinement Method
M	Freestream Mach number
NS	Navier-Stokes
OASPL	Overall Sound Pressure Level
SPL	Sound Pressure Level

Presented at the AHS 4th Decennial Specialist's Conference on Aeromechanics, San Francisco, California, January 21-23, 2004.

Introduction

Blade/vortex interaction (BVI) is one of the most challenging problems encountered in modern rotorcraft since it affects both the aerodynamic performance of rotors, as well as, the acoustic signature of the aircraft. Despite its importance, the phenomenon is not fully understood and it is still the subject of numerous experimental and theoretical investigations [1, 2, 3]. The difficulty in successfully simulating BVI stems from the fact that Computational Fluid Dynamics solvers tends to dissipate small disturbances in the flow field. Upwind and dissipative schemes work fairly well in problems where acoustic disturbances are not of interest since in most of the cases the flow physics of the problem is not altered by the inherent numerical dissipation.

In aeroacoustics problems, however, this situation is not acceptable. Not only acoustic disturbances but flow structures may be affected by the properties of numerical schemes. A well-known example is the convection of vortices where the core properties are altered during calculation. High order schemes are currently available, with better properties both in terms of acoustics and dissipation of vortices offering substantial improvements over conventional second/third order schemes. Their implementation in CFD solvers is, however, difficult and most of the times is associated with a long period of validation and in practice it may result in loss of efficiency and stability during calculation.

The present work attempts to present a method for modelling BVI using CFD and Computational Aeroacoustics (CAA). CFD is used to generate the unsteady pressure field around a blade during BVI and this is used as a source in a CAA method. Central to this effort is the Compressible Vorticity Confinement Method (CVCM) which allows traditional CFD methods to preserve vortices. CVCM is used for preserving vortices up to and beyond their interaction with the blade. Once the acoustics waves are generated very close to the surface of the blade, the Ffowes Williams-Hawkings method is used for assessing their effect on the far-field acoustics of the aircraft. The method has been validated in a sequence of simple cases starting from vortex convection and getting into inviscid and viscous calculations for a set of well-documented head-on BVI cases.

It has to be mentioned that the CVCM technique is able to help with one aspect of the problem i.e. the dissipation of vortices. It is of little help with the preservation of acoustic waves in the flow and this is something that only a high-order scheme combined with a fine discretisation grid could achieve. Near a blade, however, the computational grid is sufficiently fine to capture the acoustic waves provided the vortex in the flow is well-preserved. Using the pressure field near the blade to source, a CAA method is therefore a way of tackling the BVI problem.

It is the objective of this paper to present the validation of the method as well as the results of a parametric study revealing the characteristics of both the near-field and far-field acoustics of the phenomenon. Inviscid and viscous calculations have been carried out and the obtained results highlight the differences in the acoustic behaviour of various aerofoil sections and of vortices with different properties.

Numerical Method

CFD Solver

The PMB code of the University of Glasgow [4] is used in the present work. This is a parallel, structured, multiblock code with implicit time stepping. It uses the Osher's and Roe's schemes combined with a preconditioned Krylov solver for efficiency.

To extend the capability of the code for predicting flows with strong vortical structures the Compressible Vorticity Confinement Method (CVCM) [5] has been implemented. This method is particularly attractive since it is economic in terms of memory and CPU time and relatively simple to implement in existing solvers. This method has been successfully used for tracking vortices [6, 7] and more specifically for rotorcraft simulations [8]. Application of the method is also reported for several other flow cases including flows over complex bodies, massively separated flows and even flow visualization. Recently, it was applied to allow the simulation of blade-vortex interaction [9] which is the main focus of this paper.

The Compressible Vorticity Confinement Method

The Vorticity Confinement Method (VCM) developed by Steinhoff [10] is aimed at countering the dissipation of the numerical scheme employed in CFD. The VCM is based on the observation that the numerical scheme tends to dissipate the vortices in the flow. The basic modification is to add a body force term $\vec{\mathbf{f_b}}$ to the momentum transport equations which for incompressible flow reads:

$$\rho\frac{\partial\vec{\mathbf{V}}}{\partial t}+\rho(\vec{\mathbf{V}}.\nabla)\vec{\mathbf{V}}+\nabla p=\mu\nabla^2\vec{\mathbf{V}}-\vec{\mathbf{f_b}}. \qquad (1)$$

The body force term $\vec{\mathbf{f_b}}$ is given by $-\rho\varepsilon\frac{|\Delta\vec{\omega}|}{|\Delta|\vec{\omega}||}\times\vec{\omega}$ where ε, μ and $\vec{\omega}$ are respectively the confinement parameter, an artificial viscosity term and the vorticity.

The extension of the VCM to the compressible Navier-Stokes (NS) equations has been realised by including the work of the body source term in the energy equation [11]. The integral form of the NS equations can be rewritten for a two-dimensional problem as

$$\frac{d}{dt}\int_\vartheta W d\vartheta+\int_\Sigma F.\vec{\mathbf{n}}d\Sigma+\int_\Sigma G.\vec{\mathbf{n}}d\Sigma=-\int_\vartheta S d\vartheta. \qquad (2)$$

where W is the vector of the conservative variables, F and G are the inviscid fluxes in two spatial dimensions and the source term S can be expressed as

$$S = \left\{ \begin{array}{c} 0 \\ \varepsilon\rho\left(\vec{\mathbf{n}}\times\vec{\omega}\right).\vec{\mathbf{i}} \\ \varepsilon\rho\left(\vec{\mathbf{n}}\times\vec{\omega}\right).\vec{\mathbf{j}} \\ \varepsilon\rho\left(\vec{\mathbf{n}}\times\vec{\omega}\right).\vec{\mathbf{V}} \end{array} \right\} with \left\{ \begin{array}{c} \vec{\mathbf{n}} = \frac{\nabla|\vec{\omega}|}{|\nabla|\vec{\omega}||} \\ \vec{\omega} = \frac{\vec{\partial}}{\partial\mathbf{M}} \times \vec{\mathbf{V}} \end{array} \right. . \quad (3)$$

The term $-\rho\varepsilon\frac{|\Delta\omega|}{|\Delta|\omega||}\times\omega$ is added to the transport equations of the momentum components, while ε, ρ and ω represent the confinement parameter, the density and the vorticity, respectively. In order to include the work done by the body source term in the energy conservation law, the term $-\varepsilon\rho\left(\vec{\mathbf{n}}\times\vec{\omega}\right)$ also contributes as a part of the residual. A complete review of the Compressible Vorticity Confinement Method is given in the thesis by Hu [12].

The implementation of the method in the PMB solver as well as the selection of the optimum scheme for scaling the confinement parameter ε are presented in [9].

Computational Aeroacoustics Method

Two different approaches are common for determining the farfield noise: the Kirchhoff method [13] and the Ffowes Williams-Hawkings (FW-H) [14].

The use of the Kirchhoff method requires that all the non-linearities of the flow are inside a control surface which is supposed to be representative of the flow phenomena occurring during the BVI. In this case, using Green's theorem, it is possible to calculate exactly the pressure distribution outside the surface. The method also requires knowledge of the time history of the flow quantities. Although the method is easy to adopt in potential-like flows, cases with strong vortices traveling in the flow domain or cases with higher Mach number require a larger surface since the nonlinearities prevail longer in all spatial directions [15]. This is a hard requirement to be met since CFD methods loose resolution of the flow field in coarse grids far away of the main area of interest in the flow. This implies that a judicious choice of the Kirchhoff surface [16] is necessary. As reported by Brentner [17], the Kirchhoff approach for moving surfaces can lead to erroneous results for two reasons. First, the integrations over the control surface do not represent the physics of the BVI when the vortex passes through the surface and predictions can be misleading unless the integration surface is large enough to include the vortex before or during the interaction. Furthermore, the Kirchhoff method requires the use of a nearfield which is usually distant by at least one chord from the aerofoil to include the non-linear effects of the flow on the acoustics. This makes the Kirchhoff method unreliable for most CFD solvers which tend to dissipate the pressure waves unless adaptive grid refinement or/and high-order spatial schemes are used to preserve the acoustical waves for longer. Nevertheless, the determination of the farfield noise remains possible with the use of the FW-H method [18] which can be formulated to include surface properties only.

At subsonic flow, the FW-H method has the advantage of only requiring the accurate prediction of the loads on a lifting surface and even though the surface has to be carefully chosen when simulating transonic BVI, little difference in the region of maximum BVI noise intensity was noticed by Singh and Baeder [19] when quadrupole noise is neglected. The FH-W method also decomposes the noise into different sources making the analysis of the obtained results easier. The BVI is then classified as an impulsive loading noise. Due to the above reasons the FW-H method has gained popularity and it is possible to predict the thickness and loading noises from the FW-H equations provided the surface loads are known [20].

Regardless of choice, both FW-H and Kirchhoff methods rely on the accuracy of the nearfield acoustics which in this work is obtained from CFD calculations. Therefore, the ability of the CFD solver for preserving acoustic waves needs to be investigated. As shown in Figure 1, acoustic signals dissipate fast, which should not happen. So, despite the fact that the CVCM is capable of conserving vorticity, it does not help the preservation of the acoustical waves. This implies that only the near-field close to the aerofoil which is correctly captured by CFD can be used as input data. Since the loads history can be well-predicted with the use of the CVCM, the FW-H is preferred for the study of the farfield noise. As in most acoustic codes based on the FW-H formulation [21], our approach considers the linear thickness and loading terms of the FW-H equation, neglecting the non-linear quadrupole term.

Following Farassat's 1A formulation [22, 23] which is suitable for moving bodies such as helicopter blades and assuming the blades are rigid, the FW-H equation can be reformulated as follows:

$$\begin{aligned} 4\pi P'\left(\vec{x},t\right) = & \frac{1}{a}\frac{\partial}{\partial t}\int_{f=0}\left[\frac{\rho_0 c v_n + L_r}{r\left(1-M_r\right)}\right]_{ret} d\Sigma \\ & + \int_{f=0}\left[\frac{L_r}{r^2\left(1-M_r\right)}\right]_{ret} d\Sigma \end{aligned} \quad (4)$$

In the Farassat formulation 1A, it is possible to use the retarded time as a reference:

$$\left(\frac{\partial}{\partial t}\right)_x = \left[\left(\frac{1}{1-M_r}\frac{\partial}{\partial\tau}\right)_x\right]_{ret} \quad (5)$$

Then the loading and thickness acoustic pressure P'_L and P'_T are deduced from Equations 4 and 5. Their respective expression is

$$\begin{aligned} 4\pi P'_L\left(\vec{x},t\right) = & \frac{1}{a}\int_{f=0}\left[\frac{\dot{L}_i\hat{r}_i}{r\left(1-M_r\right)^2}\right]_{ret} d\Sigma \\ & I \\ & + \int_{f=0}\left[\frac{L_r - L_i M_i}{r^2\left(1-M_r\right)^2}\right]_{ret} d\Sigma \\ & II \end{aligned} \quad (6)$$

$$+\frac{1}{a}\int_{f=0}\left[\frac{L_r\left(r\dot{M}_i\hat{r}_i+cM_r-cM^2\right)}{r^2\left(1-M_r\right)^3}\right]_{ret}d\Sigma$$

$$III$$

$$4\pi P_T^{'}\left(\vec{x},t\right)=$$
$$\frac{1}{a}\int_{f=0}\left[\frac{\rho_o v_n\left(r\dot{M}_i\hat{r}_i+cM_r-cM^2\right)}{r^2\left(1-M_r\right)^3}\right]_{ret}d\Sigma \quad (7)$$

The acoustic pressure is expressed as the sum of the loading and thickness noise sources:

$$P^{'}\left(\vec{x},t\right)=P_L^{'}\left(\vec{x},t\right)+P_T^{'}\left(\vec{x},t\right) \quad (8)$$

The thickness term [24] which considers the disturbance of the fluid medium caused by the airfoil is determined by the blade characteristics and the forward velocities. The loading terms which represents the noise caused by the airfoil exerting a force on the fluid [25] requires the calculation of the forces acting on the blade.

It is interesting to note that "the loading noise depends on the projection of the forces onto the direction from the blade to the observer" [22]. Term I is supposed to be the dominant term of the loading noise. Therefore, only term I of Equation 6 is estimated. Note that the distance aircraft-observer was also approximated so that the aircraft was seen as a source point.

According to [22], only subsonic motion of the blade is allowed, i.e, for low forward speed (20m/s). Discrepancies appear in the prediction at high forward speeds (V=67m/s) due to the large contribution of the quadrupolar noise [26] for higher tip Mach numbers, which is created by the velocity perturbation along the blade chord. Furthermore, the presence of shocks, i.e. strong discontinuity in pressure, are also a possible source of noise. Both quadrupole and shock noise are assumed to be at the origin of the noise discrepancy.

For acoustic prediction, the integration of the lift force (term I of Equation 4) over the chordwise direction is often realised assuming that the blade can be seen as a point source ($r/c << 1$). The force is then applied at the quarter chord and the BVI is said to be chordwise compact [27]. The compactness of the chordwise loading distribution is justified as long as the aspect ratio of the blade is high and the flow which is considered 2D locally make the frequency range of BVI low enough for the observer not to perceive any chordwise variations [26]. Indeed, the generation of an acoustic wave is associated with a particular phase [28]. Each section wave can be characterised by a phase which corresponds to a fixed section of the blade. The radiated noise therefore depends on the phase delay between all the acoustic pressures for a fixed chordwise section, which implies that the noise levels may be overpredicted.

The modification of the phase delay is also an important parameter of the BVI noise generation since BVI acoustic phasing influences the directionality of the radiated noise [29]. A comparison between the non-compact and the compact modeling has been undertaken by Sim and Schmitz [27]. They found that a lower peak value and a larger acoustic pulse width is obtained for the compact modeling. However, the difference in terms of noise levels between the two methods appears especially near the plane of the rotor and decreases underneath it. Although non-compact chord assumptions does not overpredict the noise levels as the compact does, the directivity patterns or trends of the noise remains similar.

Parametric study

The complex flowfield encountered during BVI is known to produce a very intense impulsive noise [30]. As mentioned in [31], this noise has four main contributions: (i) from the vortex at subsonic speed with its upwash or downwash velocity component, (ii) from the stall and reattachment of the flow when the vortex approaches the aerofoil, (iii) from the oscillation of the stagnation point due to the high pressure region generated at the leading-edge (LE) of the aerofoil (compressibility waves) and (iv) from the development of a supersonic area at the shoulder of the aerofoil (transonic waves). It is known that the magnitude of the BVI noise and its directivity patterns are related to the aerofoil shape, the freestream Mach number, the vortex core radius, the vortex strength and the miss-distance between the vortex core and the surface of the aerofoil. Using the combined CFD/CAA method described above, a study has been conducted in order to investigate the influence of each of the above mentioned parameters on BVI. A list of the conditions along with the nature of the calculations is given in Table 1.

Head-on BVI has been simulated for six different aerofoils at subsonic and transonic flow conditions: NACA-0006, NACA-0012, NACA-0018, NACA-001234, NACA16018 and SC-1095 (see Figure 2). The three first sections are symmetric with increasing thickness while the fourth and the fifth ones are NACA 4-digit profiles with a modified leading edge radius. The last one is a cambered section and is representative of the sections currently used in helicopter rotors. For the employed sections the leading edge radius is respectively 0.397%, 1.587%, 3.57%, 0.397%, 1.587% and 0.7% of the aerofoil chord.

The range of Mach numbers under consideration was chosen to highlight the differences between subsonic and transonic flow, which explains why a high Mach number of 0.8 was chosen for the latter. The Cp, lift and drag histories of the vortex-aerofoil interaction given by Euler and NS calculations are presented for the different types of BVI at different Mach numbers. Note that the Reynolds number was fixed to one million for viscous calculations and the angle of attack was set to zero for all the calculations.

Effects of aerofoil shape at subsonic and transonic conditions

Different NACA profiles were used to highlight the role of the thickness and the LE radius of the aerofoil. Calculations were also run with the SC-1095 aerofoil to investigate the influence a cambered section may have. For this profile (SC-1095) the loaded aerofoil calculations were performed by keeping the angle of attack to 0^0. Further runs were also carried out with the aerofoil set at its zero-lift angle.

For subsonic flow, the Cp history at x/c=0.02 on the upper surface is similar for all aerofoils as shown in Figure 3. It can be seen that the LE radius has a stronger effect on the thinner aerofoils. It is expected that a smaller leading-edge should actually be more sensitive to the vortex-induced "downwash"[32], which is translated into larger fluctuations in the pressure distributions near the LE [33]. The differences on the lower side seem to be driven by the LE radius and the thickness, especially for the chordwise location x/c=0.02. This is illustrated by the Cp of the NACA-0006 and NACA-001234 aerofoils. As depicted in Figure 4(a-b), the secondary generated vortex is weaker for the NACA-001234, leading to lower Cp. Although this confirms the idea that the LE radius is more important for thinner aerofoils at subsonic flow, the overall influence of the secondary vortex on the Cp is small due to its short lifespan (see Figure 4(c-d)).

Results are now discussed for transonic flow cases at a freestream Mach number of 0.8. The history of the surface pressure coefficient is shown in Figure 5. Since the aerofoils have different shock locations, it remains difficult to assess the importance of the thickness and the LE radius. However, the BVI peaks seem to delay for thick aerofoils with large LE radius and is remarkable that the peaks do not occur at the same time due to compressibility. Note that, although the peaks of the lift coefficients are now lower than the subsonic case, the lift forces exerted on the body are in fact stronger due to the high dynamic head.

The presence of the vortex was found to affect the shock. The vortex while moving over the surface of the aerofoil encounters the shock, thickens the shock and regains some strength. This explains why the Cp curve has wider peaks. It also explains the different loading of the blades before the BVI. Indeed, the shock location on the lower side was found to move upstream, which changes the symmetry between the shocks on the lower and upper surfaces and therefore modifies the loads. For the SC-1095 aerofoil, the difference of loads before the interaction at the transonic regime mainly comes from the cambered shape of the aerofoil, the aerofoil offsetting strong shock formation.

The lift history and the lift peaks are given in Figure 6 for different aerofoils at the transonic flow. The peak of lift confirms that a small LE radius leads to higher BVI loads for thicker aerofoils at transonic flow. The thickness of the aerofoils seems also to determine the timing of occurrence of the peaks. As suggested by Hardin and Lamkin [34], and Booth [23, 35], the vortex decelerates as it approaches the aerofoil, leading to the generation of lift. It is interesting to establish a comparison between the subsonic and transonic flows for the SC-1095 aerofoil. As shown in Figure 7, the initial loading of the aerofoil has an effect on the unsteady loading both before and after the encounter with the vortex. As mentioned in [36], the lift coefficient is observed to be positive when the vortex induces a downwash at the LE of the aerofoil in both subsonic and transonic flows. Afterwards, when the vortex passes the LE, the lift coefficient rapidly increases. The drag peak increases with the strength of the shocks. As expected, the SC-1095 aerofoil has the lowest drag coefficient and, for the unloaded case, it appears to be the less affected by the BVI at the Mach number of 0.8. Note that only the integration of the lift over the time domain could give a good estimation of the influence of the LE radius and of the thickness at subsonic flow due to the small differences between the lift of the aerofoils.

So far the aerodynamics of the interaction, as characterised by the surface pressures and the lift history, have been considered. The differences in acoustics are now discussed for the different aerofoils. The high directivity of BVI noise is usually illustrated by two distinct radiation lobes. These two waves are called compressibility waves and are typical for high subsonic flow. These waves are due to the oscillation of the stagnation point induced by the passage of the vortex. This generates an enlarged high-pressure region which propagates upstream like a steepening shock wave [37]. The flow deflection at the LE of the aerofoil is actually large enough for the acoustic waves to detach from the aerofoil. The two waves are denoted by A and B in Figure 8(a, c) and once they reach the trailing-edge, two new waves start to form which propagate upstream contributing to the trailing-edge noise. The trailing-edge waves [34] are marked as C and D in Figure 8(a, c).

The acoustic pressure was calculated at four probes marked as P_1, P_2, P_3, P_4 in Figure 8(a, c) to allow a comparison of the magnitude and the phase of all acoustic waves present in the flow. The calculation was repeated for all aerofoils and at two freestream Mach numbers. Figures 8(b) and 8(d) show the typical signature of the waves, respectively at subsonic and transonic flow. The compressibility waves only pass through points P_1 and P_2 and look very similar in terms of magnitude and are opposite in phase. The same remark can be made for the transonic waves at points P_3 and P_4. It can be observed that the TE waves also pass through points P_1 and P_2. The time history of the acoustic pressure for the probe at point P_1 indicates the passage of the acoustical wave A. The acoustic behaviour of the different aerofoils in subsonic flow is similar in terms of acoustic pressure peak. The acoustic pressure of the main wave which propagates downstream is of the same level (about 3% of the freestream pressure) for the four symmetric aerofoils. However, the pressure differences encountered just after the vortex reaches the aerofoil and again as it reaches the TE seem to increase for the thinner aerofoils.

Figures 9(a-b) and 9(e-f) establish a comparison between the compressibility waves propagating above and below the aerofoil at the two flow regimes whereas Figures 9(c-d) and 9(g-h) depict the TE waves propagating upstream. It has to be noticed that there are significant differences in the strength and direction of the acoustical waves between the two Mach numbers. Despite the fact that at low Mach the passage of the vortex does not perturb the loads on the aerofoil as much as in transonic flow, the level of acoustic pressure at transonic Mach is higher than the subsonic case. The time history of the acoustic pressure through the point P_1 at high Mach differs from the subsonic one in three aspects. First, the difference of SPL for the transonic flow from the subsonic flow is about 10dB. Secondly, the acoustic waves are generated earlier after the interaction for the transonic case than for the subsonic one. Finally, the acoustic response of the aerofoils after the interaction varies with the location and strength of the shocks which are likely to make the BVI less impulsive as the vortex passes through them. The resulting directivity patterns of the radiated acoustic waves which is a result of the complex interaction between the vortex, the boundary layer and the shocks are all different. The acoustic waves seem to propagate more upstream and to be wider for thicker sections.

An additional acoustic wave is present for transonic flow. This wave, called the transonic wave emerges when a supersonic flow region is present on the shoulder of the aerofoil [37]. As explained in [31, 38], a shock wave appears after the vortex reaches the maximum thickness of the aerofoil beyond which the supersonic area collapses. Then the shock wave moves upstream leaving the LE in a downward direction while the stagnation point moves upwards. This results in the generation of a sound wave propagating upstream [39] which is marked by E. The compressibility wave propagates upstream at zero angle to the chord of the section while the transonic wave moves in a vertical downward direction [15]. As expected, the compressibility and trailing-edge wave are also present for the transonic flow case.

It is also interesting to note that the BVI magnitude seems to be related to the loading of the aerofoil, as shown by the different peaks obtained on the loaded and unloaded SC-1095 cases. The acoustical signal at point P is similar at the subsonic flow (see Figure 10(a, b)). However, the unloaded aerofoil seems to be less critical in terms of BVI noise magnitude at the transonic flow. As illustrated by Figure 10(c, d), the transonic wave E merges with the compressibility waves for the loaded aerofoil whereas both waves are more separated for the unloaded aerofoil, explaining the difference of acoustic pressure levels.

Effects of vortex properties

Vortex core radius

Calculations were run inviscid for head-on and miss-distance ($y_0 = -0.15$) BVI, and the employed grids were of 240k and 170k points, respectively. The non-dimensionalised vortex strength was set to -0.283 at a Mach number of 0.5 for the first case and to -0.42 for a Mach number of 0.73 for the last case. The radii were set to 0.018, 0.04, 0.06 and 0.10 for the head-on BVI and to 0.4, 0.06, 0.10 and 0.15 for the miss-distance BVI.

The surface pressure coefficients are given in Figure 11. A stronger BVI is obtained for a smaller vortex core size. For the head-on BVI, the loads seem to be more sensitive to the vortex core size, the loads magnitude being much larger for the smaller vortex. Since the vortex strength was kept the same for the different vortices, it appears that the head-on BVI strongly depends on the core radius. For the miss-distance BVI, the size of the vortex core is not as important as the head-on BVI. Although the interaction becomes stronger when the vortex core size decreases, a vortex of smaller core radius is found to have a lesser effect on the loads. This is a important difference between head-on and miss-distance BVI for non-lifting aerofoils as far as the influence of the vortex core size is regarded.

The time histories of the lift and pressure drag are shown in Figures 12 and 13. It is noticeable that the overall shape of the lift is the same for the four different core radii. The lift tends to increase for vortices of smaller radius but the overall shape of the lift curve remains the same except for the part where the interaction occurs. The apparent angle of attack induced by the vortex is larger for the vortex with the highest tangential velocity and this suggests that the induced angle is primarily a function of the vortex strength of the initial vortex. The same remarks can be made for the drag coefficient: the drag reduces more for the clockwise-rotating vortex of the smaller core radius.

The nearfield acoustics is now discussed. The non-dimensionalised pressure is given in Figure 14. For the head-on BVI, the acoustic waves are weaker and wider for vortices of initially larger core radius. Although the acoustic waves are not as wide for a given miss-distance, the vortex core size also influences the magnitude of the pressure wave with the stronger BVI obtained for the smaller radius. This is expected since the magnitude of the maximum tangential velocity is a function of the core radius to miss-distance ratio and the times of emission of the acoustical waves are different for the two freestream conditions.

Regarding the acoustic signal passing through point P, the first BVI peak due to the compressibility wave is observed for both flow cases. This is illustrated by Figure 15. However, the time history of the acoustic pressure differs afterwards. Indeed, for the first BVI, the acoustic pressure decreases towards zero after the high-pressure region near the LE is stabilised whereas a positive peak of pressure fluctuations which stems from the passage of the transonic wave occurs for the second type of BVI.

Vortex strength

The flow Mach number and the non-dimensionalised core radius were respectively fixed at 0.57 and 0.1. It is interesting that the apparent angle of attack induced by the incoming vortex is negative before the interaction and becomes positive after reaching the trailing-edge of the aerofoil. The clockwise-rotating vortex creates a downwash distribution of vertical velocity before the LE [33] and induces a upwash effect after the TE. It is possible to assimilate the pressure difference across the airfoil as the response of the flow to a decrease in angle of attack, this means that the vertical velocity field induced by the vortex is negative when approaching the aerofoil and becomes positive after it passes behind the aerofoil as explained by McCroskey and Goorjian [32]. After the vortex passes past the TE, another pulse of opposite sign is observed for the pressure at the TE [18] as shown in Figure 16.

Regarding the Cp history obtained for different vortex strengths, the amplitude of the Cp fluctuations increases with the vortex strength for all chordwise sections. It is also observed that the lift is driven by the vortex strength as depicted by Figure 17. This is also valid for the drag whose magnitude is larger for an initial stronger vortex.

The freestream Mach number was fixed to 0.57 and the non-dimensionalised core radius to 0.1. Contours of the non-dimensionalised pressure are given in Figures 18(a-d). The work of Hardin and Lambin [3] shows that the acoustic pressure is a linear function of the strength of the incoming vortex. This is verified for both compressibility and transonic waves of which amplitude increases with the vortex strength. However, the direction of propagation is modified with the increase of the vortex strength, and the compressibility waves almost propagate in directions normal to the aerofoil chord. Furthermore, the directivity patterns of the transonic waves remain similar, which confirms the observations of Ballmann and Körber [38].

The time history of the acoustic pressure at point P is shown in Figure 19. It is apparent that the magnitude of the BVI noise is related to the vortex strength. The transonic wave is clearly observable for $\hat{\Gamma} > 0.283$, this is manifested as a positive pressure peak after the main interaction. The fact that the magnitude of the transonic wave increases with the vortex strength suggests that the supersonic pocket which is at the origin of the generation of the transonic shock wave depends on the magnitude of the velocity induced by the vortex, i.e. the vortex strength.

Miss-distance

Inviscid calculations were run for two Mach numbers of 0.57 and 0.73 at different miss-distances of 0.00 c, 0.10 c, -0.15 c, -0.31 c, 0.45 c and 0.60 c. It was found that the BVI loads decrease linearly with the miss distance by about the same amount.

For the first BVI case, it was observed that the peak in terms of loads occurs earlier for the larger miss-distance BVI with the strength of the supersonic pocket directly related to the proximity of the vortex to the aerofoil. However, an increase of the miss-distance does not necessarily mean a proportional decrease of the main BVI [40]. The Cp history depicted by Figure 20 for the subsonic flow actually shows the stronger interaction for a miss-distance of -0.15 c on the upper surface of the aerofoil whereas the stronger BVI for the transonic flow is obtained for $y_0 = 0.0$.

The lift and drag histories are given in Figure 21. It is noticeable that the lift history is very similar for miss distances of $y_0 = 0.0$ and $y_0 = -0.10$. This verifies that the strongest interaction occurs for head-on BVI and for a miss-distance equal to the radius core. The miss-distance may be an interesting way of alleviating BVI as long as the distance vortex-aerofoil is maintained to a distance superior than twice the radius core size. The drag coefficient increases for both types of flow and becomes positive for the transonic flow at miss-distances $y_0 >= -0.15$. This may be due to the vortex-shock interaction since the shock may distort due to the vortex or even gain some strength. It is believed [41] that the drag forces influence the shock motion, more especially their directivity.

Both compressibility waves and transonic waves appear for the two types of BVI (see Figure 22 and 23). The acoustical waves noted A and B weaken with the miss-distance for both type of flows when the miss-distance is superior to the radius core. Indeed, the strongest BVI is expected for a miss-distance equal to the core radius. The vortex-induced downwash also affects the aerofoil at an early time for miss-distance BVI. As a result, the acoustical wave generated by miss-distance BVI starts to propagate before the one of head-on BVI. It is also interesting to note that the directivity of the two compressibility waves changes with the miss-distance. They tend to propagate more downstream and to merge with an increase of the distance aerofoil-to-vortex. As observed by Booth [23], the width of the acoustic waveform seems to be independent of the blade-to-vortex spacing. The compressibility wave is also found to merge with the transonic wave for small miss-distances. Note that the transonic wave disappears for too large miss-distances, i.e, when the generated supersonic pocket is not strong enough to detach and propagate into the farfield.

It is interesting to note that the transonic wave may be as strong or even stronger than the compressibility wave as shown in Figure 24. The strongest BVI appears to be for a miss-distance of -0.15 due to the transonic wave for case 1 (M=0.57) and for the head-on BVI due to the compressibility wave for case 2 (M=0.73).

Farfield acoustics

The acoustics module was tested against data taken from the experiments of Kitaplioglu [2]. A schematic of the experimental setup is shown in Figure 25(a) while a schematic of the blade with its polar co-ordinates is given in Figure 25(b). The angles Ψ and θ are respectively the azimuth and the elevation angles. The azimuth angle is equal to 0.0^o behind the rotorcraft and to 180^o in front of. A point whose elevation is set to -90^o is located just

beneath the rotorcraft. The flow conditions were the following: $\mu = 0.2,\ M_{tip} = 0.71,\ r/R = 0.886$ and the vortex characteristics were $\tilde{\Gamma} = -0.374,\ M = 0.63,\ R_c = 0.162$. The loads calculated by CFD were used for the prediction of the BVI noise at point 3 for the two miss-distance BVI ($y_0 = 0.0$ and $y_0 = -0.25$).

Due to the employed FW-H formulation, it was necessary to generate 3D loads from the 2D CFD results. First, the pressure signal had to be redistributed along the spanwise direction. As mentioned by [27], the inboard blade contributes very little to acoustics. Therefore, the BVI should only influence the loads for a spanwise radius of $r/R > 0.65$. Note that simple weighting functions were used for generating the chordwise loading distribution along the spanwise directions which correspond to given blade sections of a rectangular blade. Calculations were carried out so that the peak of BVI occurs at an azimuth angle of 144^o. It was observed that the time during which BVI happens is essential for predicting the correct BVI noise, which was expected since the lift force is integrated over the time domain. The number of steps for one revolution was therefore set so that the azimuth angle Ψ of the blade increases by an amount $d\Psi$ corresponding to the time step of the CFD computations. The distribution of the lift coefficient over the spanwise direction and the blade revolution is given in Figure 26 for the head-on BVI.

The acoustic pressure was calculated at point 3 (see Figure 25(a)) which is located ahead and below the aircraft. The results are shown in Figure 27 and are in good agreement with the experiments, which indicates that the BVI magnitude is correctly predicted by the aeroacoustical module as long as the duration of the BVI is respected. The computed acoustic pressure differs from the experimental one by its smoother shape. Indeed, the simulation of the BVI was carried out in 2D, meaning that the vortex was introduced ahead of the aerofoil. The vortex was affected by the presence of the aerofoil before the interaction, explaining why the computed signal is not as sharp as the one provided by the experiments. Both loading and thickness noises were calculated and as depicted by Figure 27, the slap noise dominates.

Description of the rotor flight conditions

The flight conditions were chosen to be representative of manoeuvres where BVI is likely to occur. It is known, that the advancing side BVI dominates the overall radiation pattern [27] with most of the noise directed downwards, beneath the helicopter in the direction of forward flight. As reported by Preissier *et al.* [42], the blade undergoes multiple interactions on the advancing side due to the tip vortices of the blade on the retreating side, especially at lower speeds since there are more vortices present in the rotor blade. Therefore, the advance ratio was set to a relatively low value of 0.2 for a blade of 6.2 meters of radius, the tip Mach number ranging from 0.5 to 0.8.

A non-lifting rotor based on the NACA-0012 aerofoil was chosen for most calculations. The tip-path-plane angle was also fixed to zero for a rectangular blade with a chord of around 40 cm length. Even though the local pitch angle was set to zero, it was not expected to have a large impact in terms of directivity [26] since the angle on the advancing side of an helicopter is small.

The location of the BVI was set at azimuth $\Psi = 90^o$ since it was demonstrated experimentally by Booth [35] that the most intense BVI acoustic radiation is generated between 65 and 90 degrees of azimuth angle. The Average Overall Sound Pressure Level (OASPL) was calculated at different observer positions to investigate the magnitude and the directivity patterns of the BVI noise. The observers have been positioned below and above the rotor for both advancing and retreating blades. The directivity of BVI has been highlighted using an (θ,Ψ) map which represents the OASPL of BVI for different rotational and azimuthal angles.

Although it has been shown previously that the transonic waves may be as strong or even stronger than the compressibility waves, it is assumed that they will not affect as much an observer below the rotorcraft than the compressibility waves due to the fact that they propagate upstream the aerofoil. Therefore, it is acceptable to say that the present calculations are representative of the BVI characteristics for the specified flight conditions. Note that 1024 points were sampled per rotor revolution.

Effect of the aerofoil shape

The farfield noise levels are given for an observer located 50 meters below and 50 meters ahead of the aircraft which corresponds to point P. A comparison of the acoustic pressure for the different aerofoils (see Figure 28) shows that only slight differences in terms of BVI noise magnitude appear for Mach number of 0.5, the NACA-0018 remaining the less noisy, the three others giving similar acoustical response. It is interesting to note that the unloaded SC-1095 aerofoil is slightly less noisy than the loaded SC-1095 at point P, suggesting that the induced loads affect the BVI noise directivity. The levels of thickness noise are negligible against the loading noise levels as depicted by Figure 28.

The importance of the aerofoil shape [15] is verified for transonic flow at which the behaviour of the BVI noise for the non-symmetric aerofoil SC-1095 and the NACA-0018 is different from the other NACA aerofoils as depicted by Figure 29. It was found that the noise is radiated in some preferred directions at transonic flow. The similar acoustical behaviour between the SC-1095 and NACA-0018 suggests that the camber and the movement of strong shocks which induce loads around the aerofoil modify the directivity of the BVI noise.

As no specific trends could be deduced from these aerofoils for the thickness and the LE radius which are linked together for the NACA 4-digit profiles, the NACA-001234 and the NACA-16018 aerofoils were used. It appears from Figure 30 that both LE radius and thickness do not make much of a difference in terms of noise. However, it can be observed at subsonic flow that the leading-edge radius plays a more important role for thinner aerofoils whereas

the thickness influences more the BVI magnitude for aerofoils of larger LE radius. For the transonic flow, it remained difficult to assess the role of the thickness and of the LE radius due to the difference of directivity of the aerofoils and to the necessity of using a very small time step for the CFD calculations for this head-on BVI. Nevertheless, it is suspected that the LE radius is of importance for thicker aerofoils whereas the thickness matters more for small LE radius at transonic flow.

It is observed for the two different types of flow that the AOSPL becomes a linear function of the inverse of the square distance observer-aircraft after a certain distance for different elevation angles as illustrated by Figure 31. For the transonic case, an increase of the tip Mach number also increases the amplitudes of the BVI radiation [27] through the Doppler factor [24].

Effects of vortex properties

Vortex core radius

The acoustic pressure at an observer located at point P is given in Figure 32 for different radii. Two calculations were run. The first type of BVI was head-on, the freestream Mach number and the vortex strength being respectively 0.5 and -0.283. The second BVI was set for a miss-distance of -0.15 at a Mach number of 0.73, the vortex strength was fixed to -0.42. As expected, the stronger BVI remains for the vortex of smaller radius core which is characterised by the higher tangential velocity magnitude.

It is noticeable that the decrease of the core radius affects dramatically the head-on BVI in terms of peak magnitude whereas its influence seems to decrease for the miss-distance BVI after a certain cut-off value. It is observed that the noise decreases linearly with increasing vortex core for head-on BVI as long as the radius is not too small. Regarding the miss-distance BVI, the peak of BVI noise was found to be a linear function of the vortex core size for the largest core radii (see Figure 33). The noise is less and less affected by the radius core size for small enough vortices, which is expected since the expression of the tangential velocity can then be approximated by

$$\frac{v_\theta}{V_\infty} = \frac{\hat{\Gamma}}{2\pi r} \quad for \quad R_c << r$$

This is in agreement with the observations of Malovrh, Gandhi and Tauszig [43] who reported that the changes in the vortex structure affect the BVI noise when the miss distance is less than half the blade chord.

As depicted by Figures 34, the BVI directivity patterns are more likely to enlarge for an initial vortex of larger viscous radius. Note that the BVI noise is radiated forward and downwards 60^0 beneath the rotor plane for the four aerofoils. The lobes of the head-on BVI noise get larger and the overall magnitude tends to decrease with the vortex core size. It may suggest that an increase of the radius core leads to a more spread-out radiated noise for head-on BVI. Since BVI is more likely to happen for a descending flight, i.e, when the the tip-path-plane of the rotor is tilted rearward [44], the BVI noise more often results from the interaction of the blade with an older vortex. It implies that a head-on BVI with the tip vortices may lead to a enlarged lobes of radiated noise, the core size increasing in wake age [29].

Vortex strength

The noise levels perceived by an observer located at point P for the four different types of BVI are shown in Figure 35(a). As mentioned by Lyrintzis and George [15], the disturbances increase more than linearly with the vortex strength. Indeed, a "slightly superlinear" dependence is found for the BVI peaks [16]. However, Figure 35(b) suggests that the dependence of the BVI peak on the vortex strength decreases for very strong vortices. This means that the vortex strength has to be significantly reduced [43] to alleviate the peaks in the loads.

The directivity of the BVI noise is related to compressibility effects. Head-on BVI propagates more uniformly for a stronger initial vortex as shown by the size of the lobes of the radiated noise of Figure 36.

Miss-distance

Results are discussed for two types of BVI. The first BVI was simulated at a Mach number of 0.73 for an initial vortex of non-dimensionalised strength -0.42. The second case was for a Mach number of 0.57 with a vortex strength -1.8. The non-dimensionalised radius R_c of the initial vortex was fixed to 0.1. BVI amplitude shows a linear dependence on the miss-distance [16] as long as the miss-distance is superiour to R_c (see Figure 37). It is observed that the BVI noise is inversely proportional to the miss-distance [29]. Note that the maximum BVI noise occurs when the miss-distance is equal to the vortex core size.

However, the SPL fall-off-rate with core radius gets smaller when the core radius is less than the miss distance [24]. In addition, the linear dependence of the BVI noise with the miss-distance is not valid any more for miss-distances superiour to the vortex core size for the second BVI as shown in Figure 38. The interaction between the vortex and the generated supersonic pocket may be at the origin of this behaviour.

The insensitivity to small miss-distance increases for larger vortex core radii [43]. It means that the reduction of the noise levels passes by the decrease of the velocities induced on the rotor blade [24]. Then it is more effective for reducing the BVI noise to increase the miss distance than the core radius since the vortex core size has only a strong influence on the BVI noise for head-on BVI.

Figure 39 shows the BVI trends for head-on and miss-distance BVI. It appears that the size of lobes of radiated noise increases with the miss-distances, the OASPL decreasing. It just means that the BVI noise energy is more spread-out in the case of increasing miss-distances.

Unsteady case	Parameter	M	y_0	$\hat{\Gamma}$	R_c	*Aerofoil*
Viscous	Aerofoil Shape	0.5 0.8	0.0	-0.283 -0.177	0.018	NACA-0006 NACA-0012 NACA-0018 SC-1095 NACA-01234 NACA-16018
Inviscid	Vortex core radius	0.5	0.0	-0.283	0.018 0.04 0.06 0.10	NACA-0012
		0.73	-0.15	-0.42	0.04 0.06 0.10 0.15	NACA-0012
Inviscid	Vortex strength	0.57	0.0	-0.248 -0.538 -1.16 -1.8	0.1	NACA-0012
Inviscid	Miss-distance	0.57 0.73	0.0 -0.10 -0.15 -0.31 -0.45 -0.60	-1.80 -0.42	0.1	NACA-0012

Table 1: List of the parameters examined. M, R_c, $\hat{\Gamma}$, (x_0, y_0) represent respectively the freestream Mach number, the vortex core radius non-dimensionalised against the chord, the vortex strength non-dimensionalised against the product freestream velocity-chord and the miss-distance non-dimensionalised against the chord. A number of 0.8 was chosen to highlight the differences of behaviour for the different aerofoils. Note that a negative strength $\hat{\Gamma}$ corresponds to a clockwise-rotating vortex.

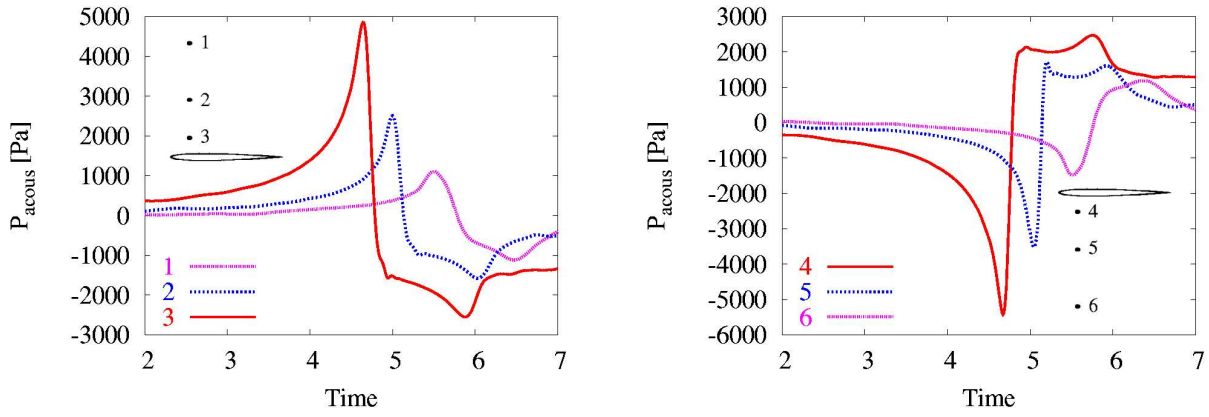

(a) (b)

Figure 1: (a) Acoustic pressure history at points 1, 2, 3 above the aerofoil - (b) Acoustic pressure history at points 4, 5, 6 below the aerofoil. Head-on BVI problem, NACA-0012 aerofoil, viscous calculations, M=0.5. $\hat{\Gamma} = -0.283$, $R_c = 0.018$.

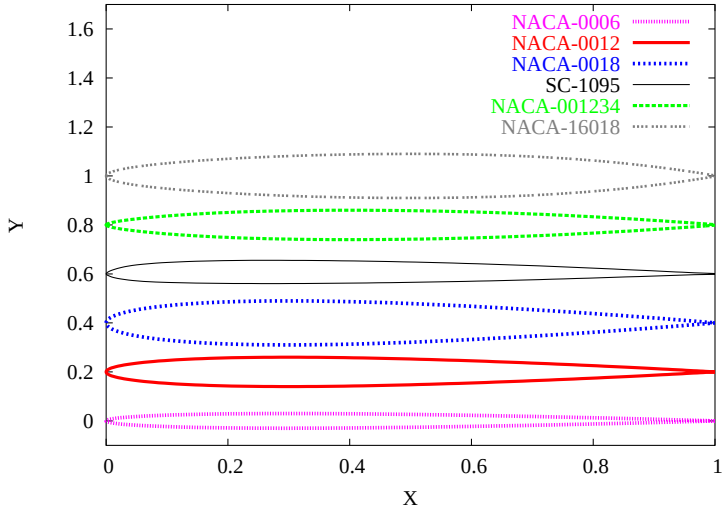

Figure 2: Geometry of the different aerofoils. The aerofoils NACA-0012, NACA-0018, SC-1095, NACA-001234 and NACA16018 are respectively offset by 0.2, 0.4, 0.6, 0.8 and 1.0 for clarity.

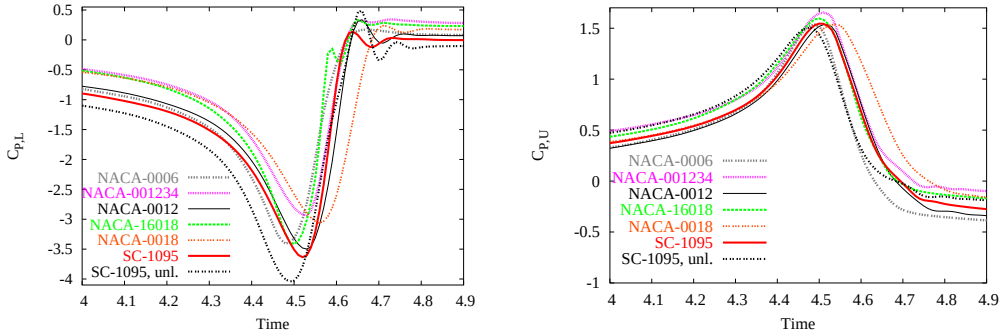

(a) Lower surface - x/c=0.02 (b) Upper surface - x/c=0.02

Figure 3: Time history of the surface pressure coefficient at different chordwise locations. Head-on BVI problem, six different aerofoils, viscous calculations, M=0.5, $\hat{\Gamma} = -0.283$, $R_c = 0.018$.

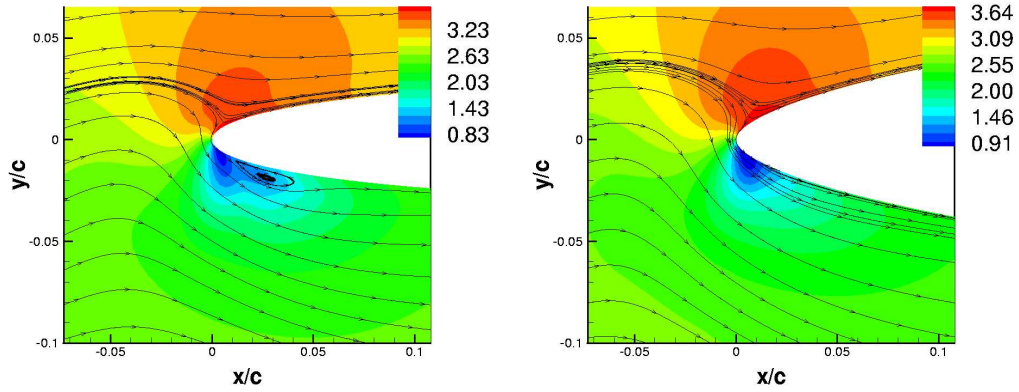

(a) NACA-0006 (b) NACA-001234

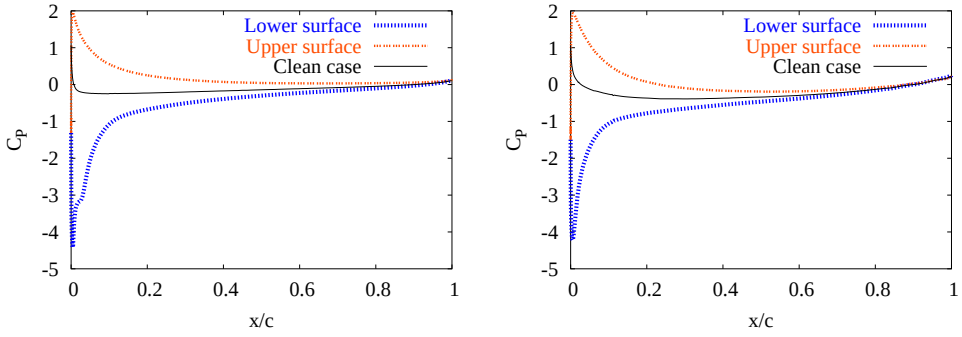

(c) NACA-0006 (d) NACA-001234

Figure 4: (a-b) Isobars (p/q_∞) along with the velocity streamlines for the NACA-0006 and NACA-001234 aerofoils. (c-d) Surface pressure coefficient at time $t\,(U_\infty/c)$=4.51. Head-on BVI, viscous calculations, M=0.5. $\hat{\Gamma} = -0.283$, $R_c = 0.018$.

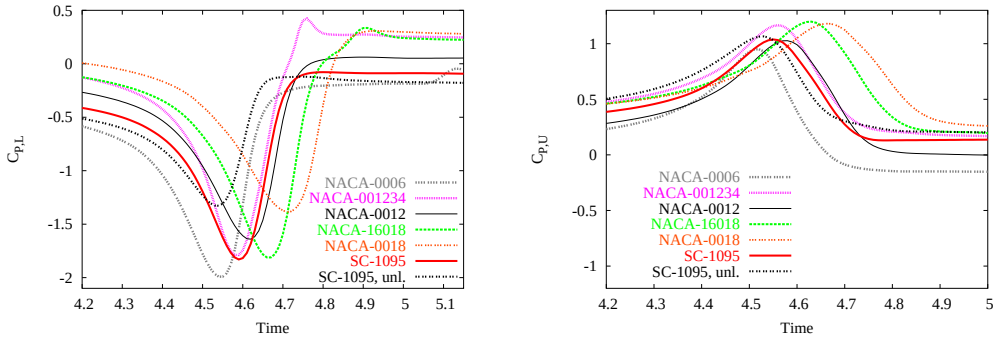

(a) Lower surface - x/c=0.02 (b) Upper surface - x/c=0.02

Figure 5: Time history of the surface pressure coefficient at different chordwise locations. Head-on BVI problem, six different aerofoils, viscous calculations, M=0.8, $\hat{\Gamma} = -0.177$, $R_c = 0.018$.

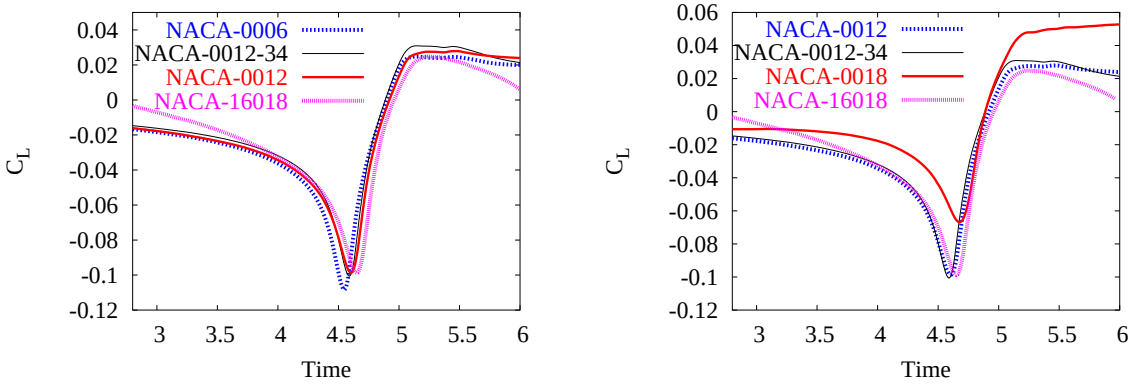

(a) Same LE radius (b) Same thickness

Figure 6: Time history of the lift for different aerofoils of the same thickness or the same LE radius at freestream Mach number 0.8. $\hat{\Gamma} = -0.177$, $R_c = 0.018$.

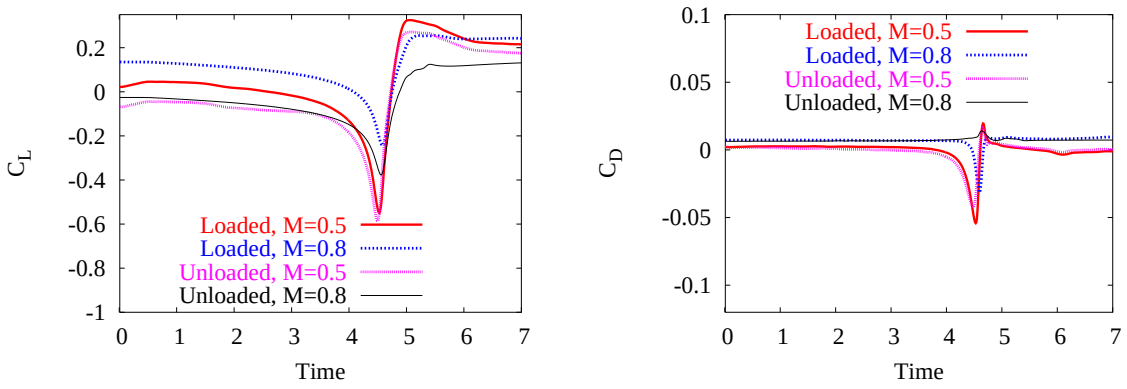

(a) (b)

Figure 7: Time histories of the lift and drag coefficients at Mach numbers of 0.5 (a) and 0.8 (b) for the loaded and unloaded SC-1095 aerofoil. $\hat{\Gamma} = -0.283$ (M=0.5), $R_c = 0.018$. Note that the drag is non-dimensionalised against $\rho_\infty U_\infty^2 c$.

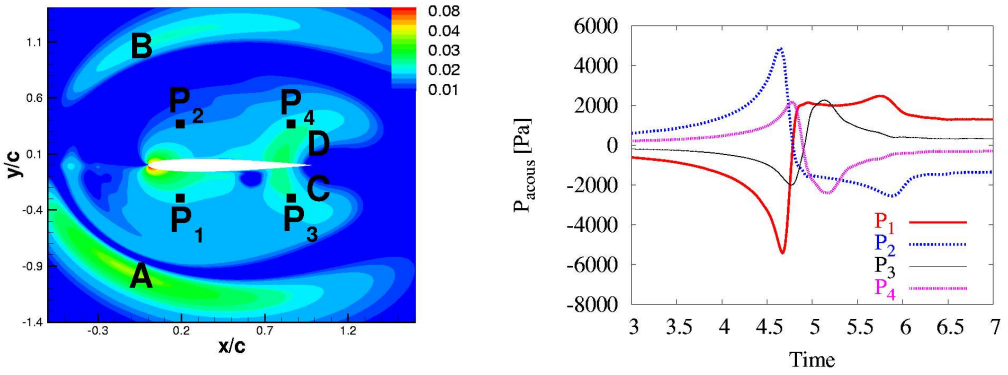

(a) M=0.5, $t\,(U_\infty/c) = 5.1$ (b) M=0.5

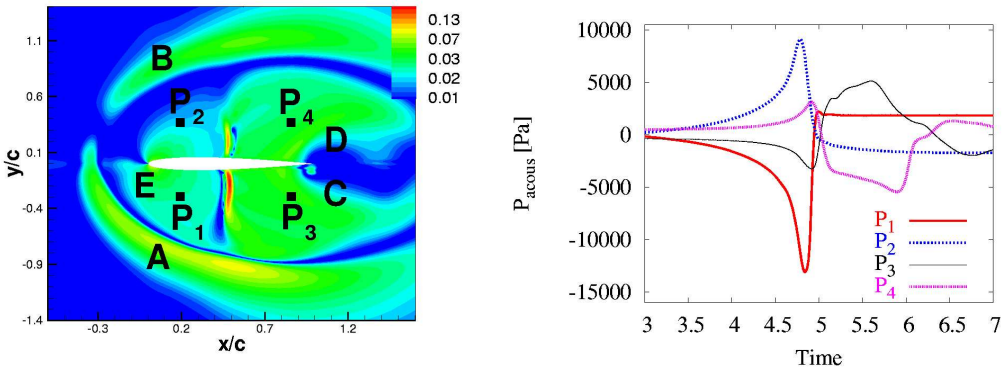

(c) M=0.8, $t\,(U_\infty/c) = 5.4$ (d) M=0.8

Figure 8: (a, c) Contours of the acoustic pressure along with the location of the four probes and (b, d) time history of the acoustic pressure at the probes. The absolute value of the acoustic pressure is represented for the NACA-0012 at a freestream Mach number of 0.5 (a, b) and 0.8 (c, d). The scale is exponential.

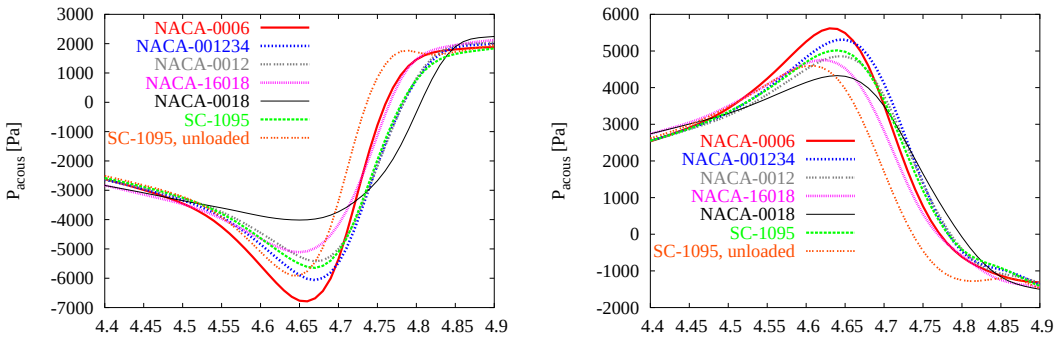

(a) M=0.5, point P_1

(b) M=0.5, point P_2

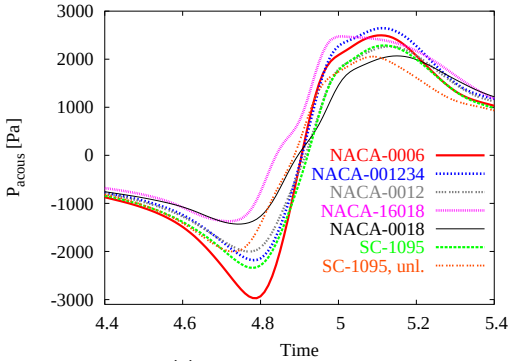

(c) M=0.5, point P_3

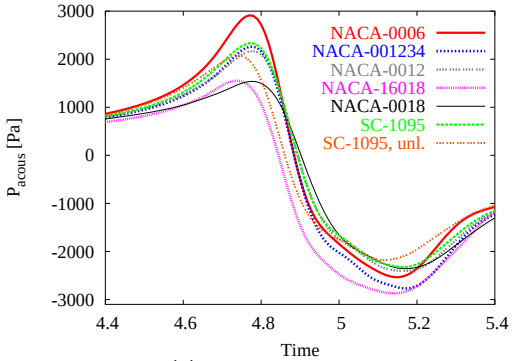

(d) M=0.5, point P_4

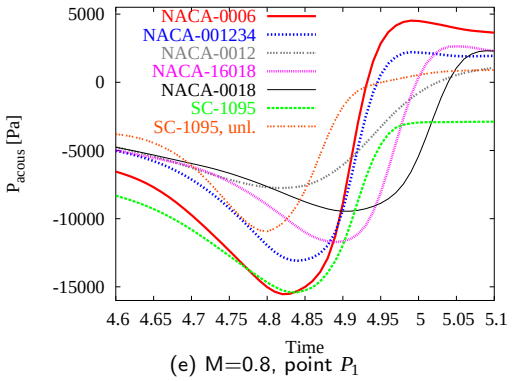

(e) M=0.8, point P_1

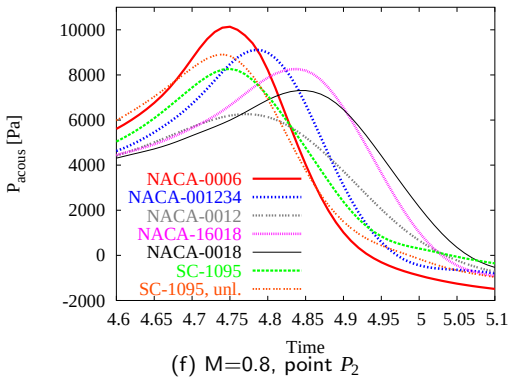

(f) M=0.8, point P_2

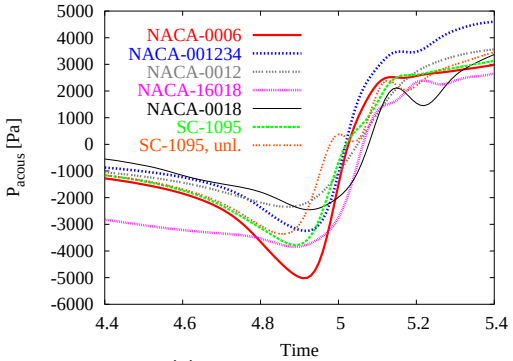

(g) M=0.8, point P_3

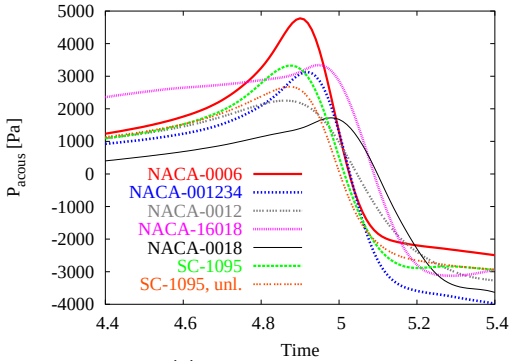

(h) M=0.8, point P_4

Figure 9: Acoustic pressure history for the aerofoils at points P_1 (a, e), P_2 (b, f), P_3 (c, g) and P_4 (d, h). Head-on BVI, $R_c = 0.018$, (a-d) Mach=0.5, $\hat{\Gamma} = -0.283$, (e-h) Mach=0.8, $\hat{\Gamma} = -0.177$.

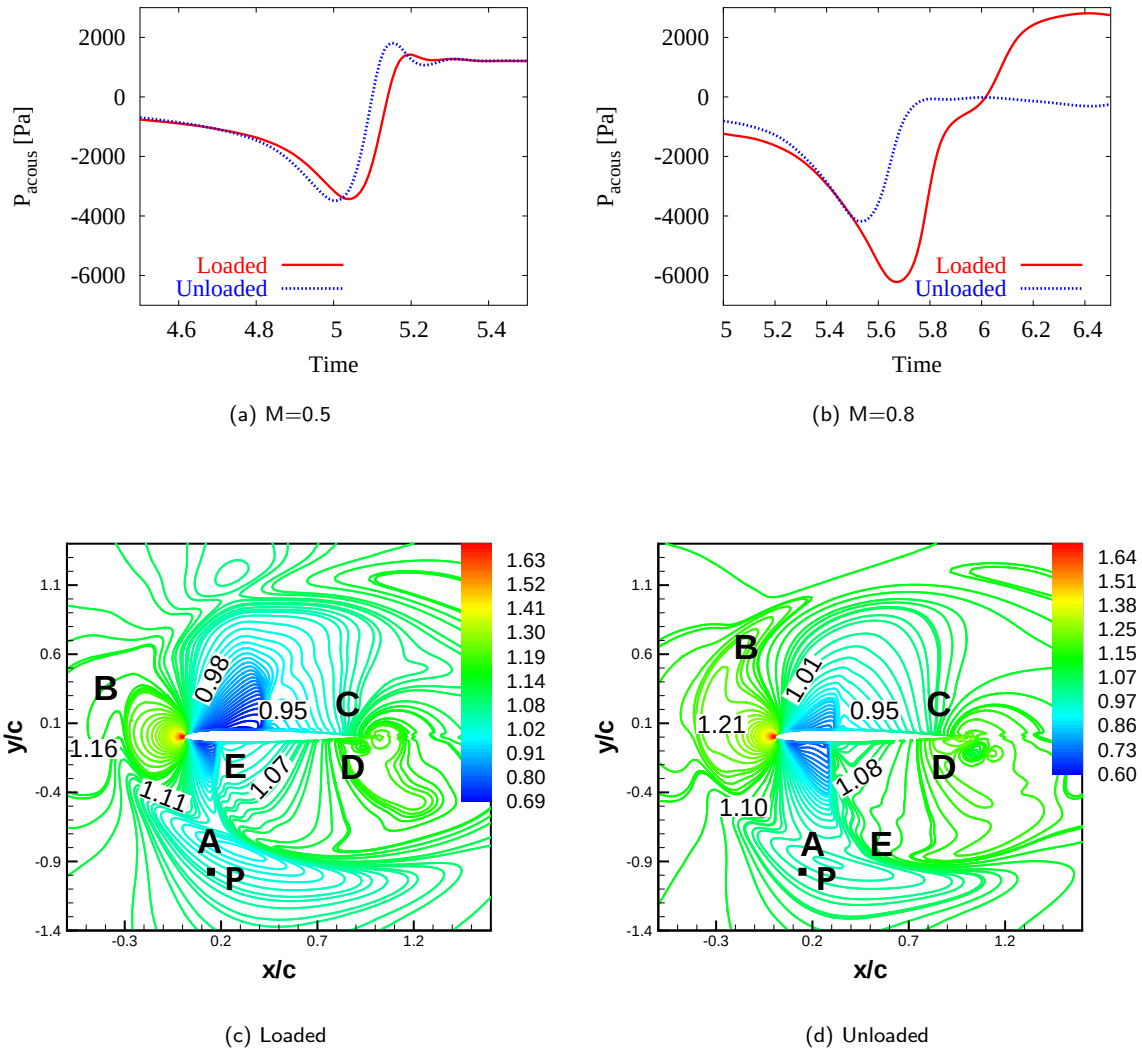

(a) M=0.5

(b) M=0.8

(c) Loaded

(d) Unloaded

Figure 10: (a-b) Acoustic pressure history at point P at two freestream Mach numbers. (c-d) Isobars (p/q_∞) at $t\,(U_\infty/c)$=5.40 the loaded (c) and unloaded (d) SC-1095 aerofoil. Viscous calculations, head-on BVI case, M=0.8, $\hat{\Gamma} = -0.177$, $R_c = 0.018$.

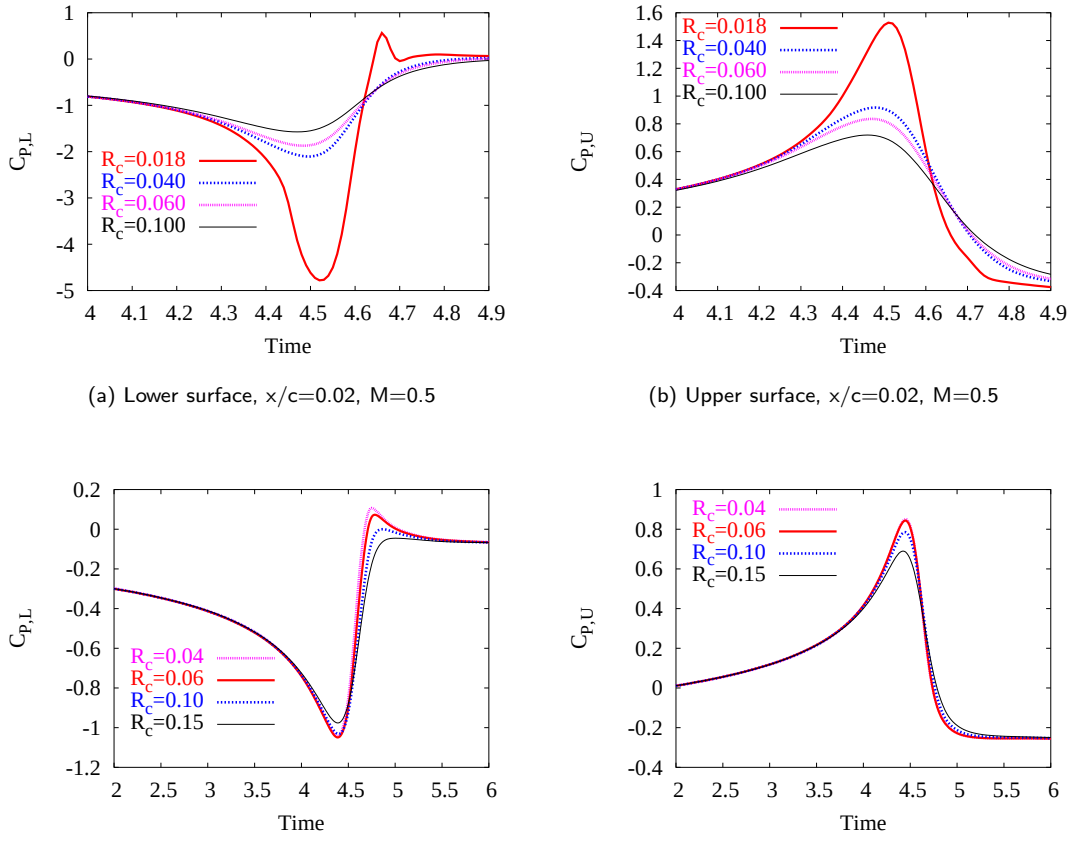

(a) Lower surface, x/c=0.02, M=0.5

(b) Upper surface, x/c=0.02, M=0.5

(c) Lower surface, x/c=0.02, M=0.73

(d) Upper surface, x/c=0.02, M=0.73

Figure 11: Time history of the surface pressure coefficient at the chordwise location x/c=0.02. Head-on BVI problem, NACA-0012 aerofoil, inviscid calculations, (a, b) M=0.5, $\hat{\Gamma} = -0.283$, $y_0 = 0.00$. (c, d) M=0.73, $\hat{\Gamma} = -0.42$, $y_0 = -0.15$.

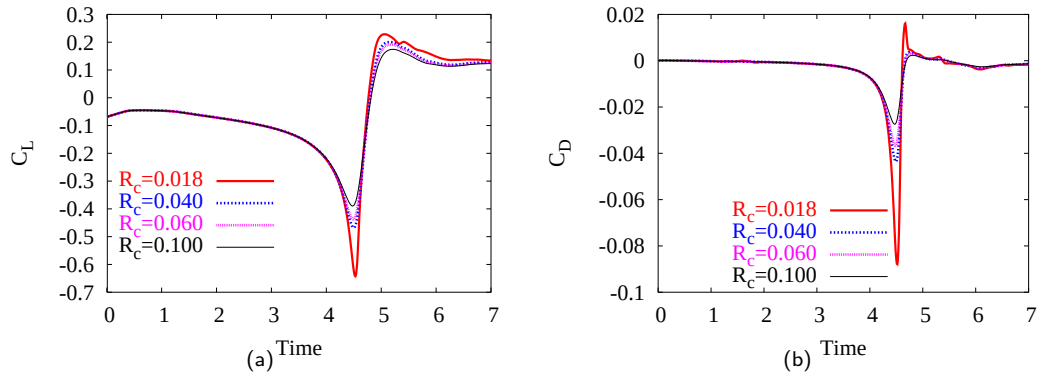

(a) Time

(b) Time

Figure 12: Time histories of the lift and drag for four vortices of different initial core radius. Head-on BVI, NACA-0012, inviscid calculations, M=0.5, $\hat{\Gamma} = -0.283$, (a) $y_0 = 0.0$, (b) $y_0 = -0.15$.

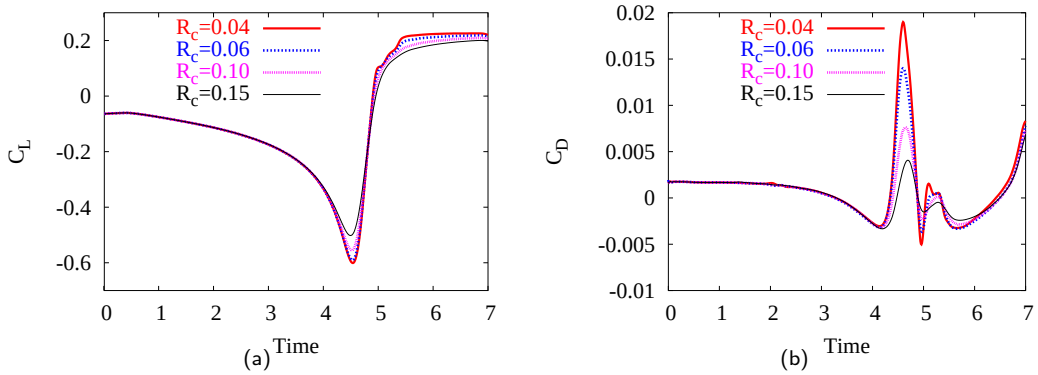

Figure 13: Time histories of the lift and drag for four vortices of different initial core radius. Head-on BVI, NACA-0012, inviscid calculations, M=0.73, $\hat{\Gamma} = -0.42$, $y0 = -0.15$.

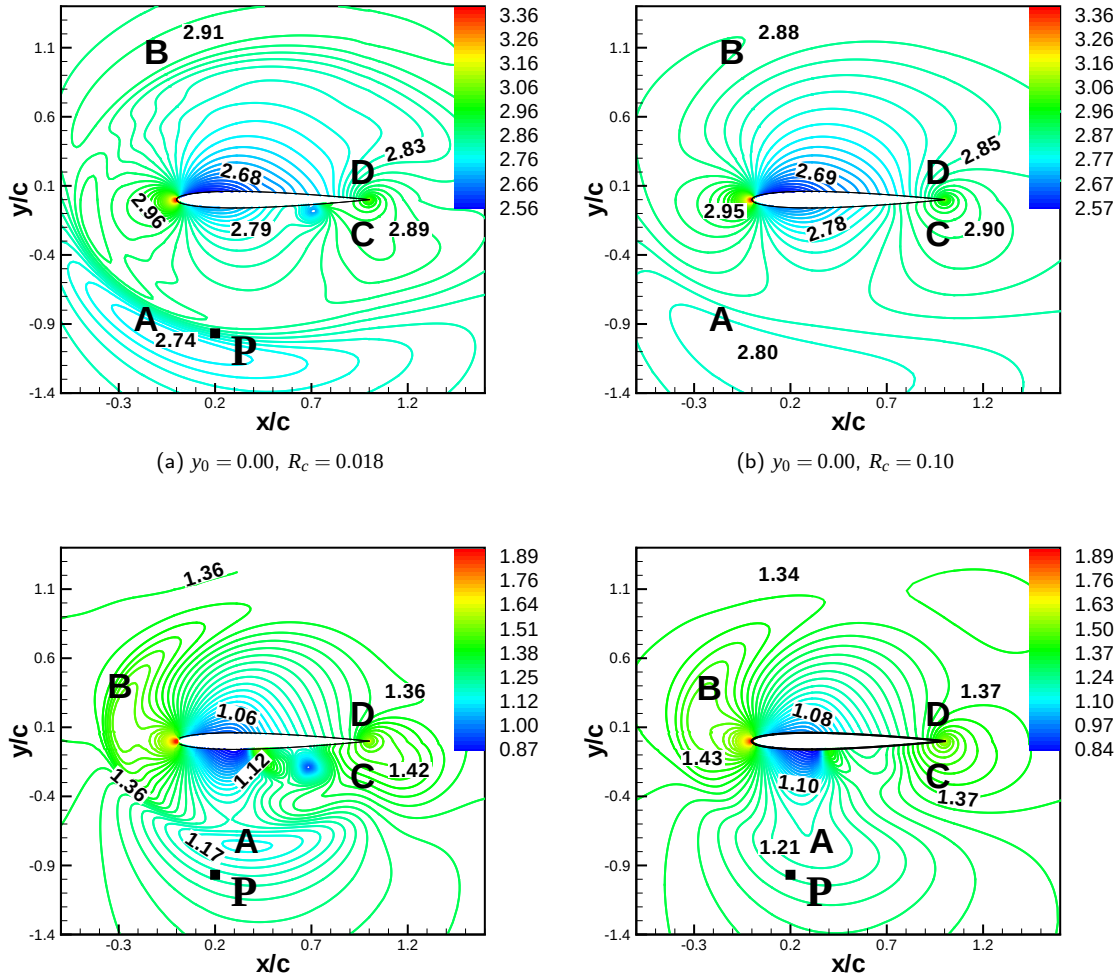

(a) $y_0 = 0.00$, $R_c = 0.018$

(b) $y_0 = 0.00$, $R_c = 0.10$

(c) $y_0 = -0.15$, $R_c = 0.04$

(d) $y_0 = -0.15$, $R_c = 0.10$

Figure 14: Isobars (p/q_∞) at $t\,(U_\infty/c)$=5.10 for different core radii. (a, b) M=0.5, $\hat{\Gamma} = -0.283$, $y_0 = 0.0$. (c, d) M=0.73, $\hat{\Gamma} = -0.42$, $y_0 = -0.15$.

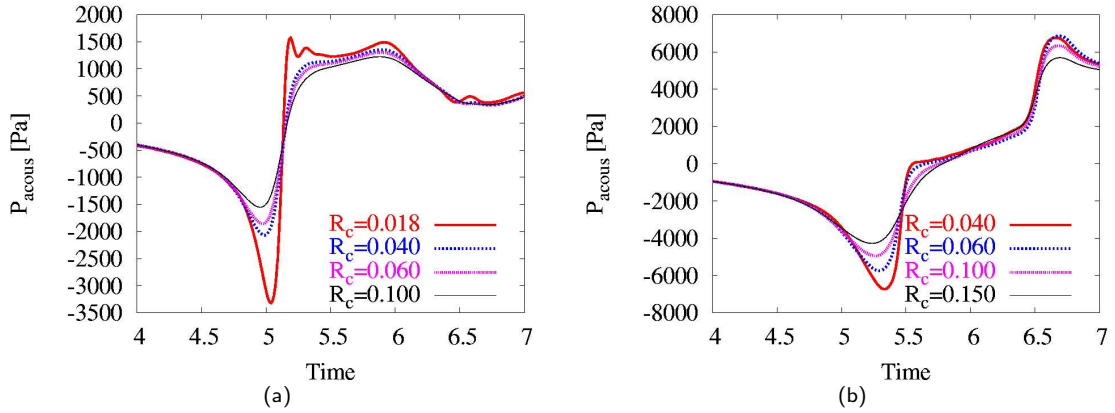

Figure 15: Acoustic pressure history at point P at two Mach numbers. (b) M=0.57, (d) M=0.73

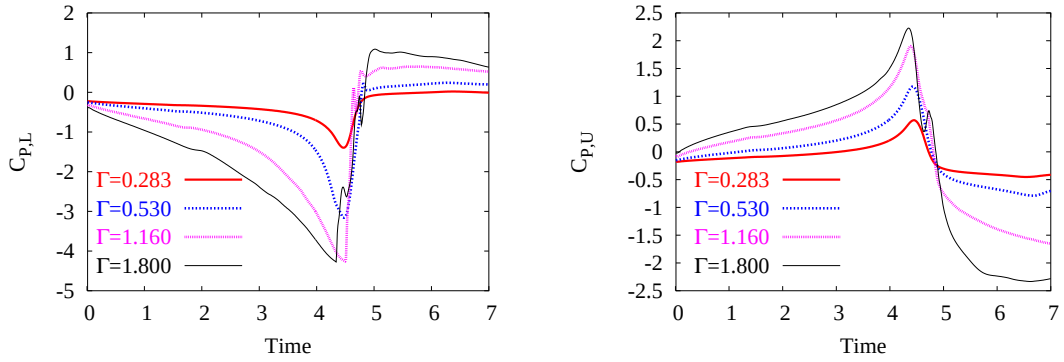

(a) Lower surface, x/c=0.02

(b) Upper surface, x/c=0.02

Figure 16: Time history of the surface pressure coefficient at the chordwise location x/c=0.02 for vortices of different strengths. Head-on BVI problem, NACA-0012 aerofoil, inviscid calculations, M=0.57. Note that the vortex strengths are non-dimensionalised against $(U_\infty c)$.

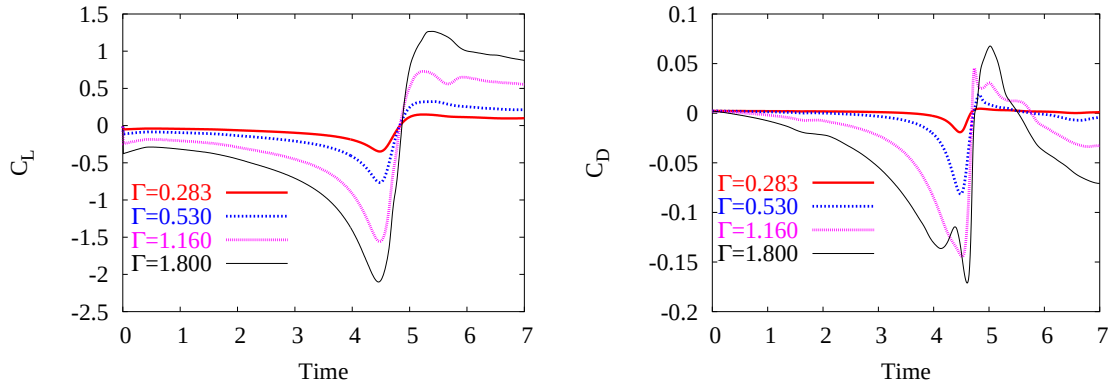

Figure 17: Lift and drag histories for vortices of different strengths. NACA-0012, head-on BVI, M=0.57, $R_c = 0.018$. Note that the vortex strengths are non-dimensionalised against $(U_\infty c)$.

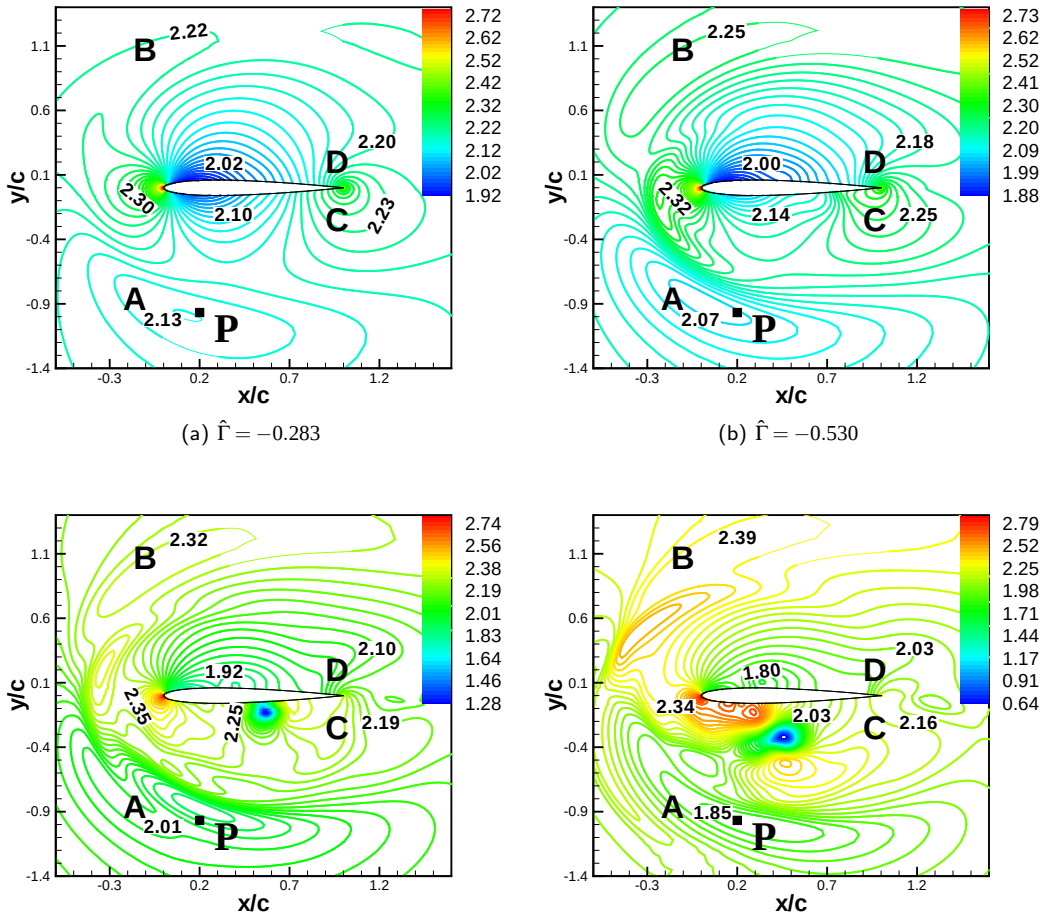

(a) $\hat{\Gamma} = -0.283$ (b) $\hat{\Gamma} = -0.530$

(c) $\hat{\Gamma} = -1.160$ (d) $\hat{\Gamma} = -1.800$

Figure 18: Isobars (p/q_∞) at $t\,(U_\infty/c)$=5.10 for vortices of different strengths. Head-on BVI, NACA-0012, Mach number of 0.5.

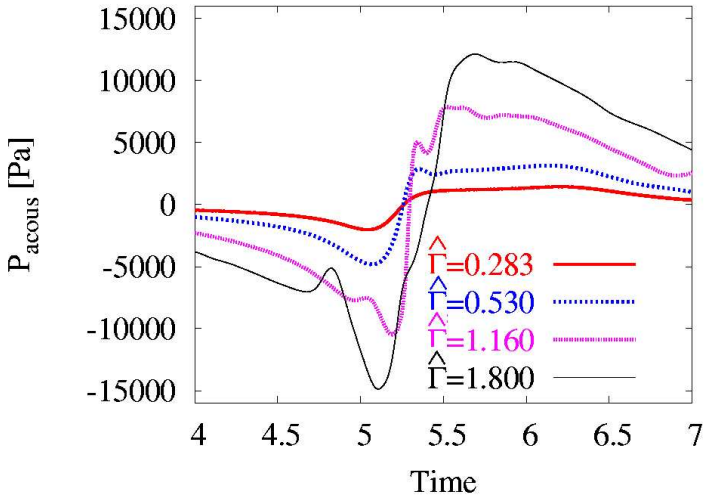

Figure 19: Acoustic pressure history at point P for clockwise-rotating vortices of different strengths. NACA-0012, M=0.57, $R_c = 0.10$.

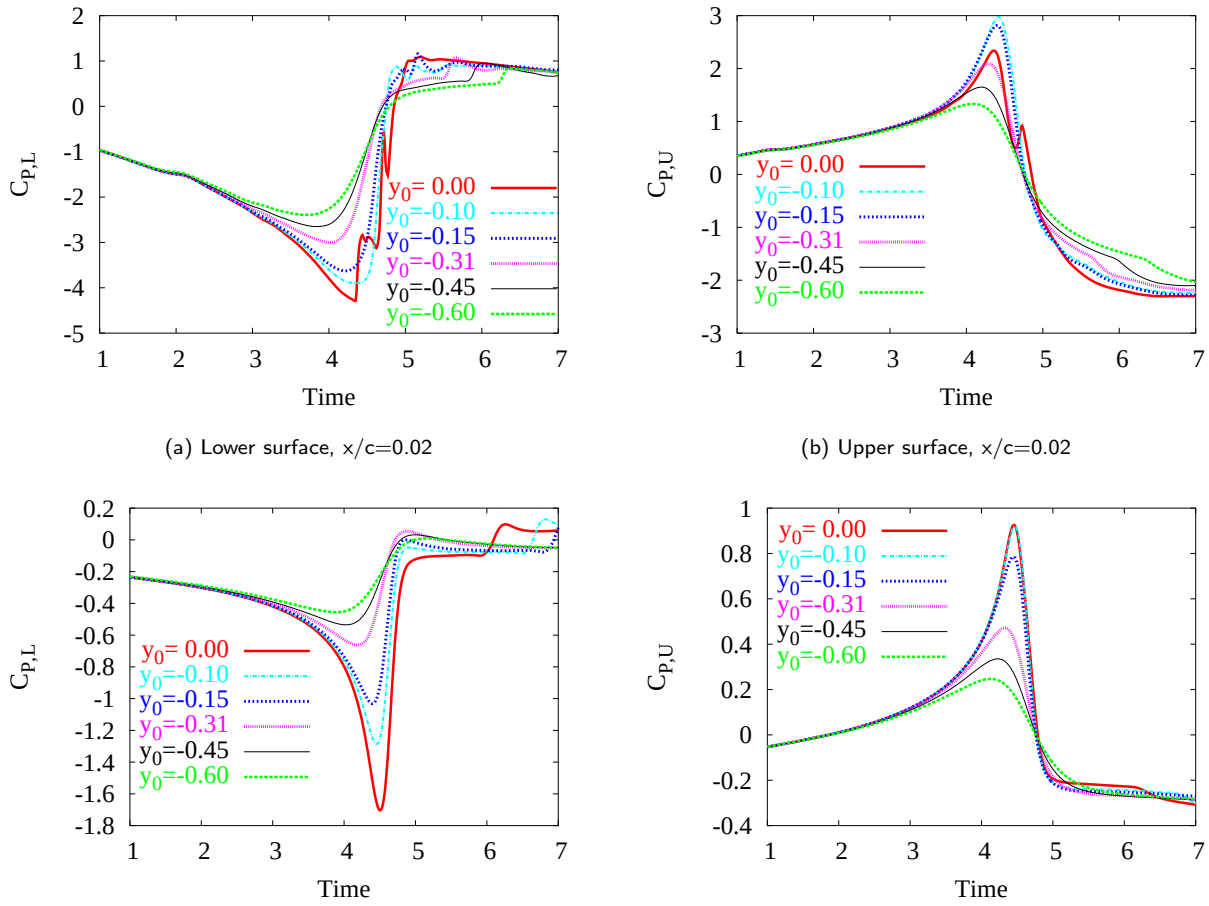

(a) Lower surface, x/c=0.02

(b) Upper surface, x/c=0.02

(c) Lower surface, x/c=0.02

(d) Upper surface, x/c=0.02

Figure 20: Time history of the surface pressure coefficient at the chordwise location x/c=0.02 for different miss-distances. Head-on BVI problem, NACA-0012 aerofoil, inviscid calculations. (a-b) Mach number of 0.57, (c-d) Mach number of 0.73.

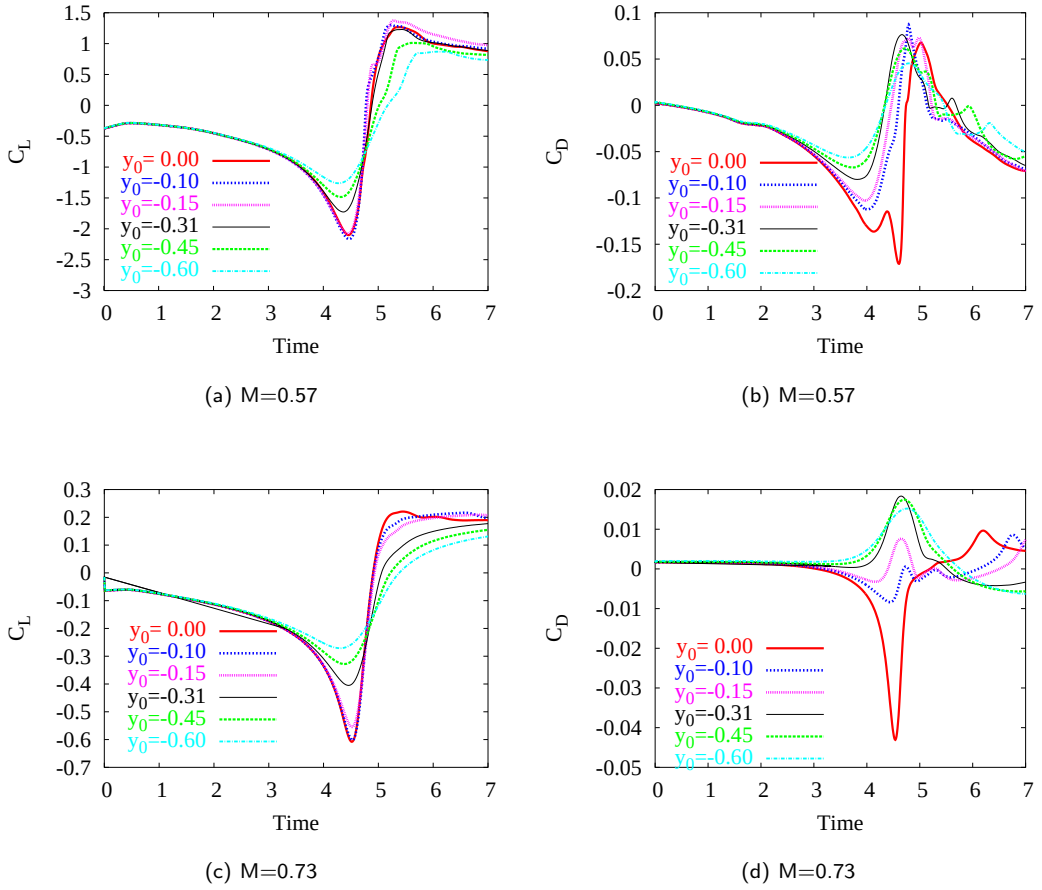

(a) M=0.57 (b) M=0.57

(c) M=0.73 (d) M=0.73

Figure 21: Lift and drag histories for vortex of various miss-distances at two flow conditions. NACA-0012. (a-b) Head-on BVI, (c-d) Miss-distance BVI.

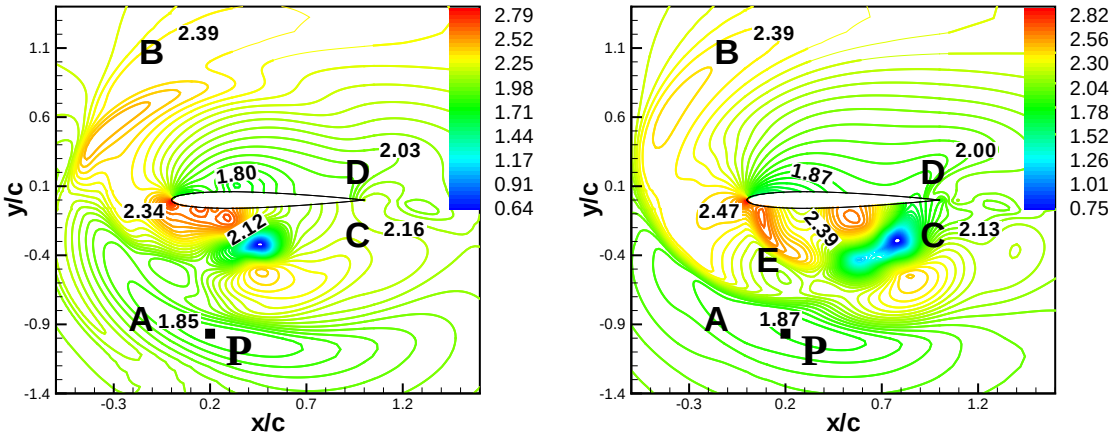

(a) $y_0 = 0.00$ (b) $y_0 = -0.15$

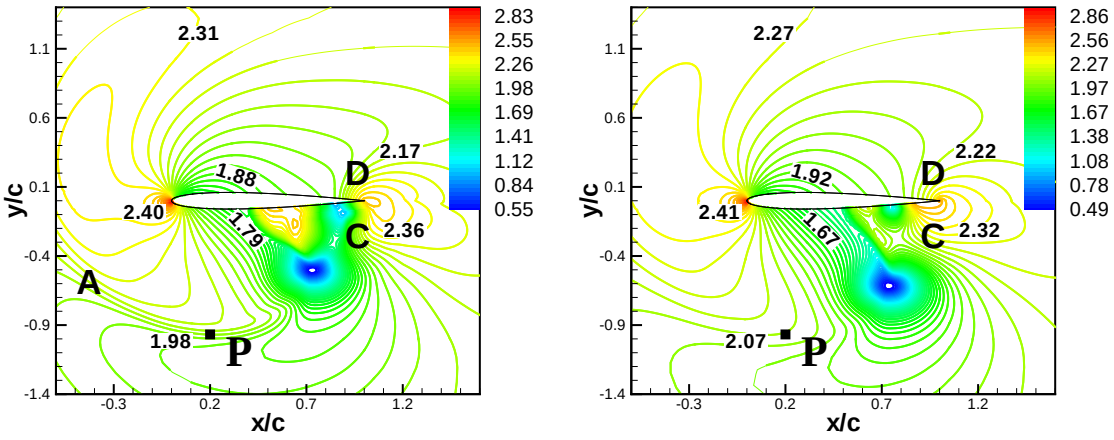

(c) $y_0 = -0.45$ (d) $y_0 = -0.60$

Figure 22: Isobars (p/q_∞) at $t\,(U_\infty/c)$=5.10. NACA-0012, Mach number of 0.57.

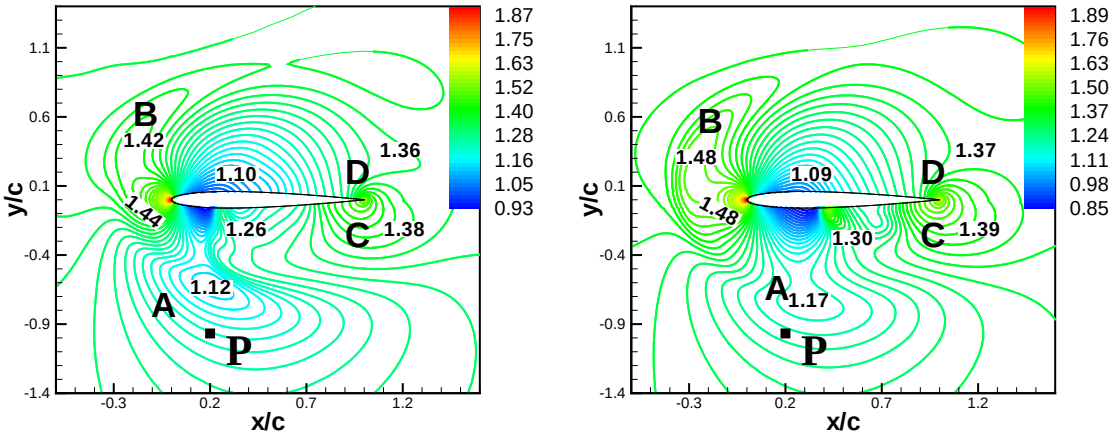

(a) $y_0 = 0.00$ (b) $y_0 = -0.15$

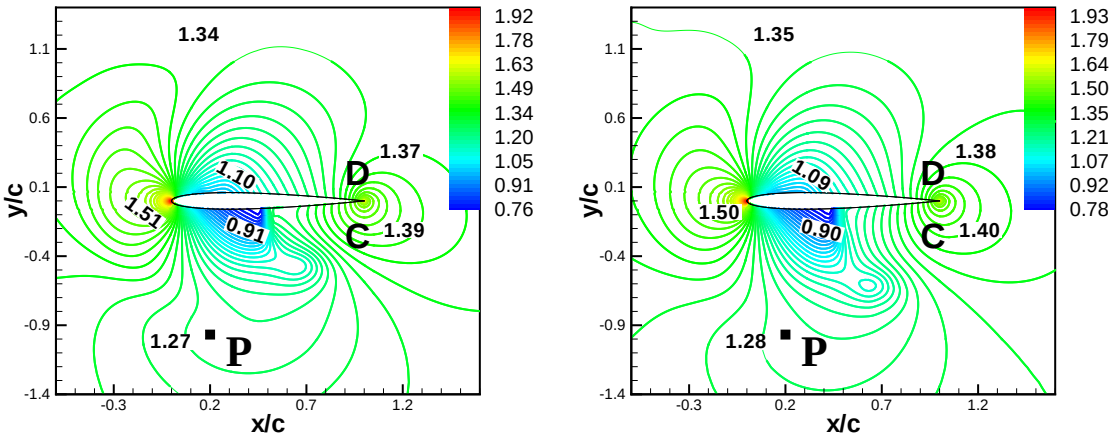

(c) $y_0 = -0.45$ (d) $y_0 = -0.60$

Figure 23: Isobars (p/q_∞) at $t\,(U_\infty/c)$=5.10. NACA-0012 and Mach number of 0.73..

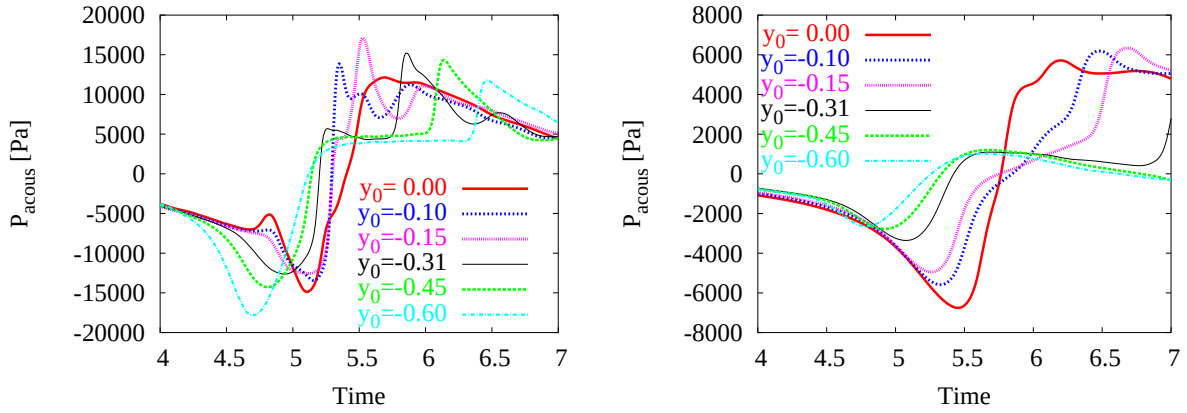

(a) Case 1

(b) Case 2

Figure 24: Acoustic pressure history at point P at two freestream Mach numbers. (a) M=0.57 , (b) M=0.73. NACA-0012, inviscid calculations, various miss-distances.

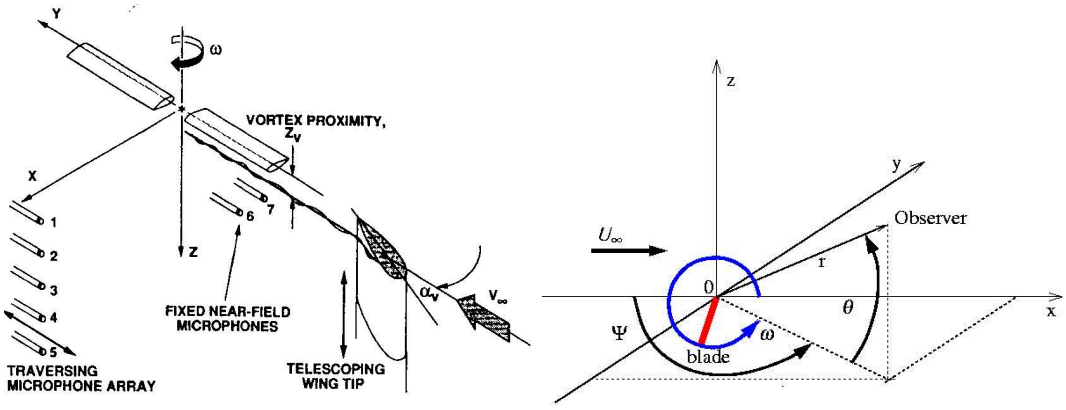

(a)

(b)

Figure 25: (a) Schematic of the BVI rotor test. (b) Schematic of the blade with its polar co-ordinates. The blade rotates anti-clockwise at $\omega/(2\pi)$ revolutions per second. The spherical co-ordinates of the observer are (r, θ, Ψ).

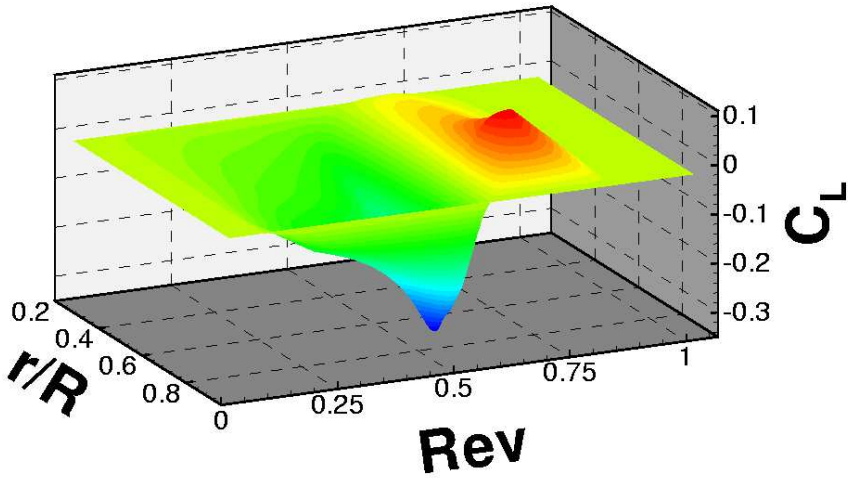

Figure 26: Distribution of the lift along the spanwise direction against the revolution of the blade. NACA-0012, head-on BVI.

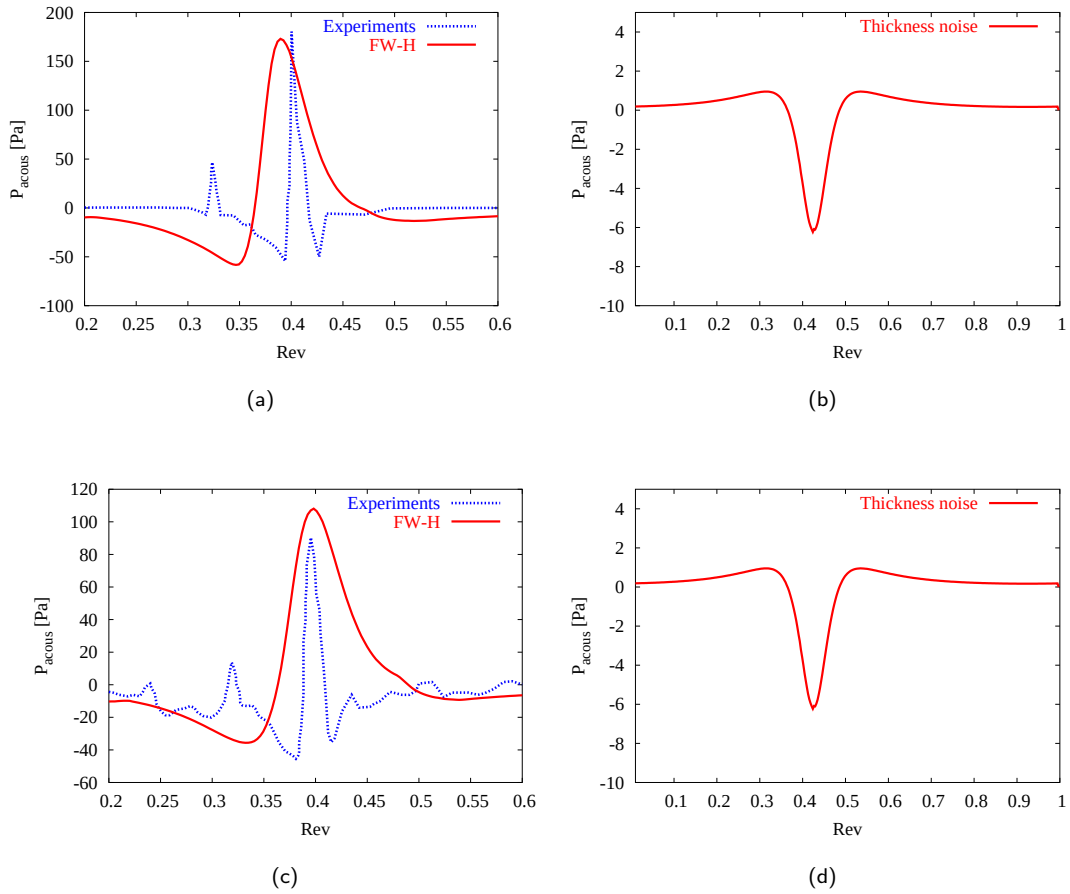

Figure 27: Acoustic pressure corresponding to the loading and thickness noises for the head-on BVI (a-b) and the miss-distance BVI (c-d). Mach=0.63, $\hat{\Gamma} = -0.374$, $R_c = 0.162$.

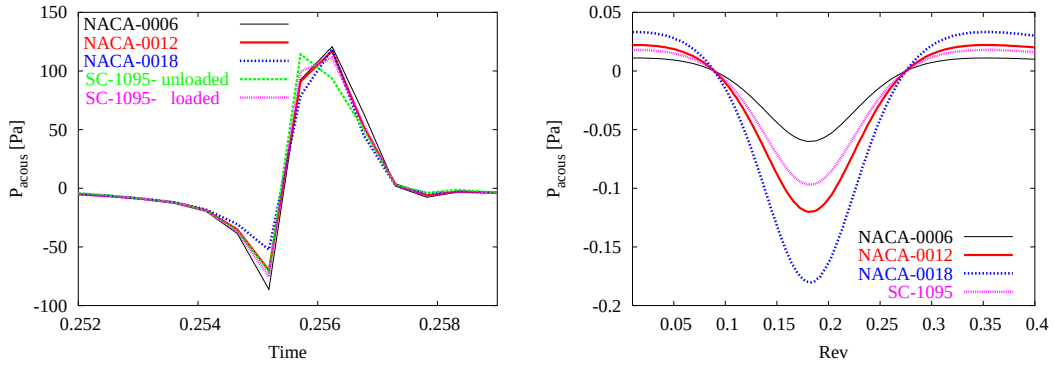

(a) Slap noise (b) Thickness noise

Figure 28: Acoustic pressure for different aerofoils at point P (50.0,0.0,-50.0). (a) Slap noise, (b) thickness noise. M=0.5, $\hat{\Gamma} = -0.283$, $R_c = 0.018$.

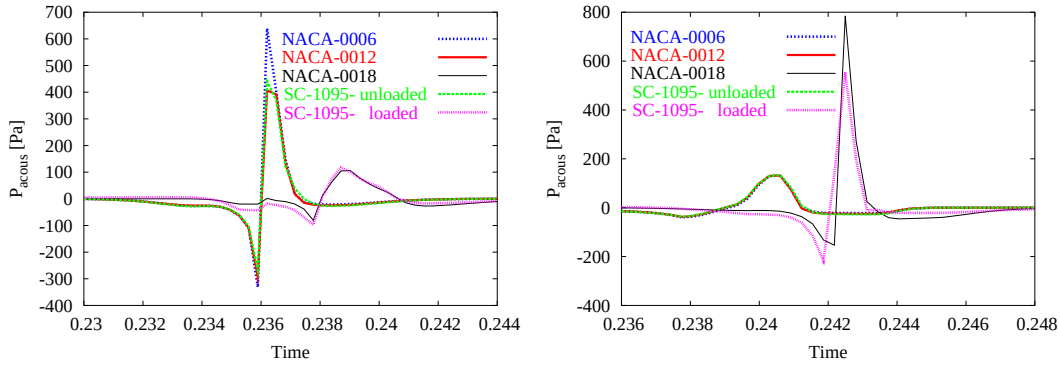

(a) (b)

Figure 29: (a) Acoustic pressure for different aerofoils at point P (50.0,0.0,-50). Results correspond to an azimuth angle of 180^o. (b) Acoustic pressure for different aerofoils at point $P^{'}$ (47.0,17.1,-50.0). Results correspond to an azimuth angle of 200^o. The distance aircraft-observer is the same as point P. M=0.8, $\hat{\Gamma} = -0.177$, $R_c = 0.018$.

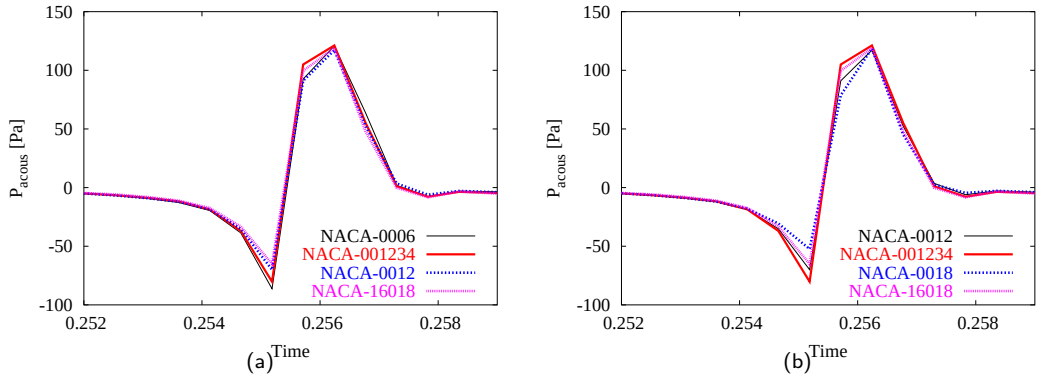

(a) (b)

Figure 30: Acoustic pressure at point (50,0,-50) for different thicknesses (a-b) and LE radii (c-d) of aerofoil. M=0.5, $\hat{\Gamma} = -0.283$, $R_c = 0.018$.

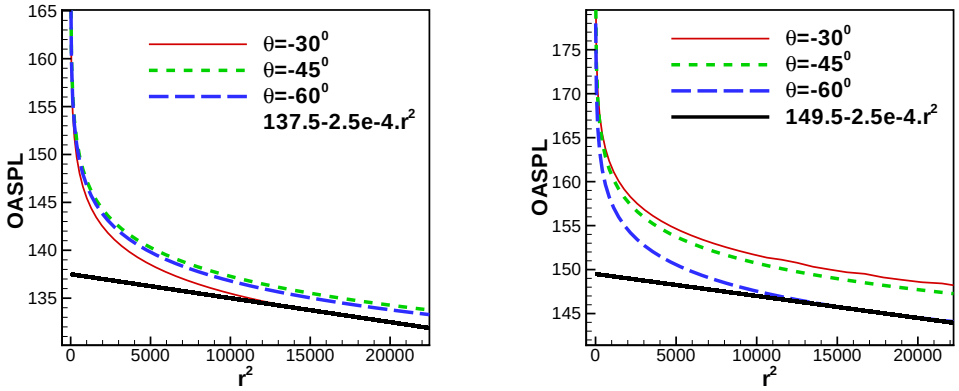

(a) M=0.5 (b) M=0.8

Figure 31: Evolution of the AOSPL against the square of the distance observer-aircraft at $\Psi = 180^o$ for three different elevation angles at two freestream Mach numbers. NACA-0012, (a) M=0.5, (b) M=0.8.

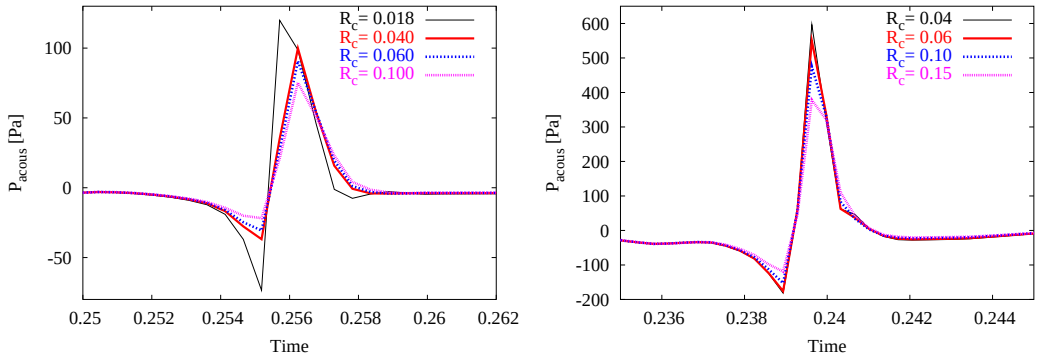

(a) M=0.5 (b) M=0.73

Figure 32: Acoustic pressure for different vortex core radii at point P (50.0,0.0,-50.0) for the head-on and miss-distance BVI. (a) $\hat{\Gamma} = -0.283$, M=0.5 for the head-on BVI, (b) $\hat{\Gamma} = -0.42$, $y_0 = -0.15$, M=0.73 for the miss-distance BVI.

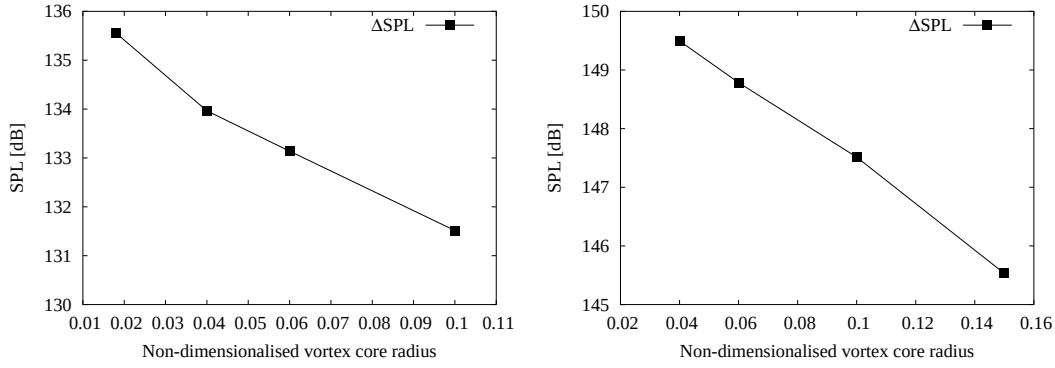

(a) M=0.5 (b) M=0.73

Figure 33: Maximum BVI noise amplitude in terms of Sound Pressure Level for different vortex core radii at two flow conditions.

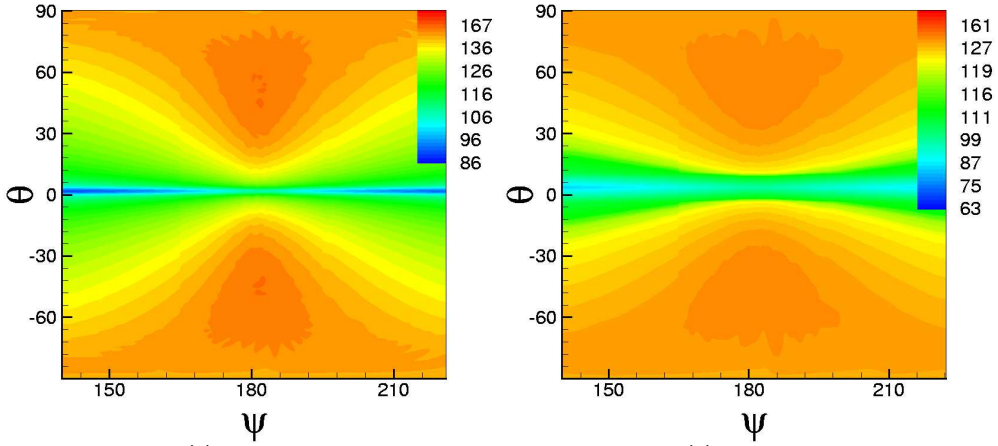

(a) R_c=0.018 (b) R_c=0.100

Figure 34: Contours of the OASPL for the range of azimuth angles Ψ where the BVI occurs. The elevation angle θ indicates the directivity patterns of the BVI noise below ($\theta < 0$) and above ($\theta > 0$) the helicopter. NACA-0012, M=0.5, (a) R_c=0.018, (b) R_c=0.100.

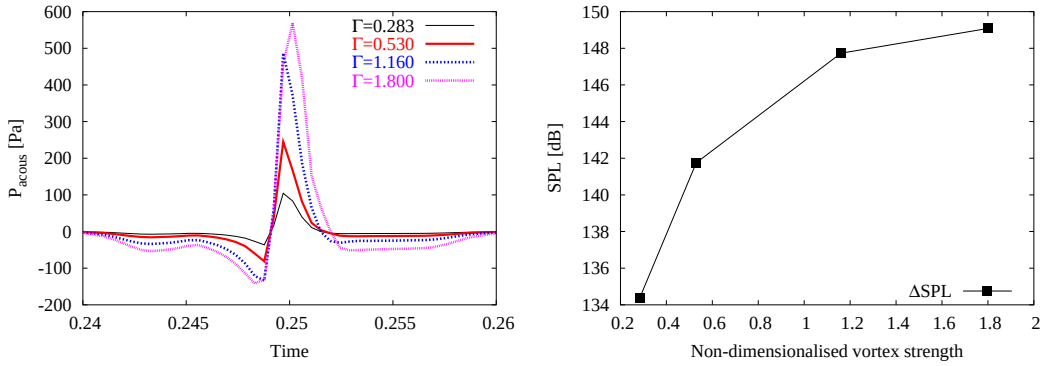

Figure 35: (a) Acoustic pressure for different aerofoils at point P (50.0,0.0,-50.0). (b) Maximum BVI noise amplitude in terms of Sound Pressure Level for different vortex strengths.

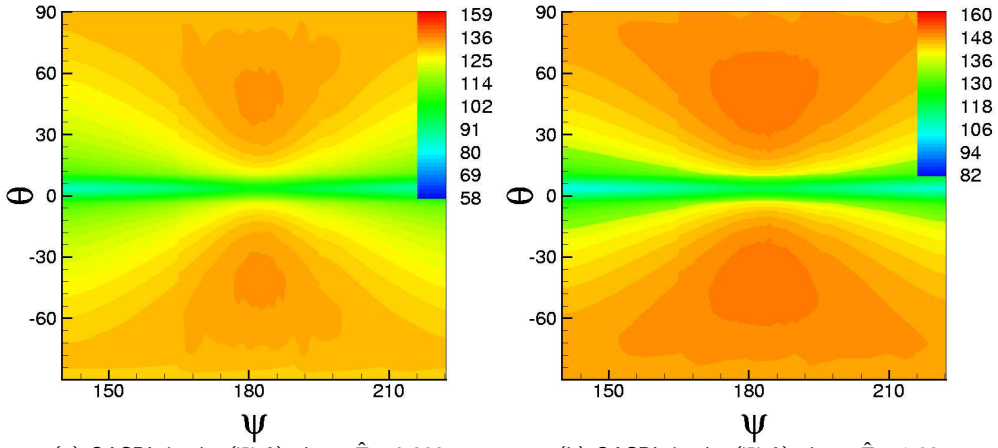

(a) OASPL in the (Ψ, θ) plane, $\hat{\Gamma}$=-0.283 (b) OASPL in the (Ψ, θ) plane, $\hat{\Gamma}$=-1.80

Figure 36: Contours of the OASPL for the range of azimuth angles Ψ where the BVI occurs. The elevation angle θ indicates the directivity patterns of the BVI noise below ($\theta < 0$) and above ($\theta > 0$) the helicopter. NACA-0012, (a) $\hat{\Gamma}$=-0.283, M=0.57 - (b) $\hat{\Gamma}$=-1.80, M=0.57.

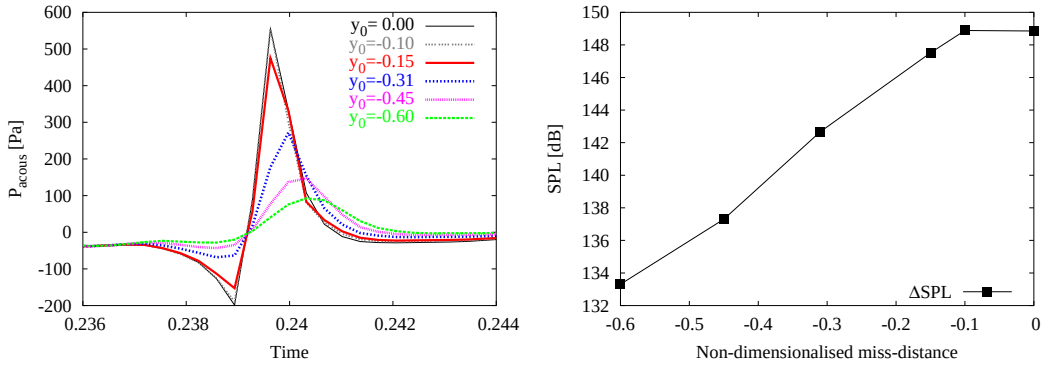

(a) (b)

Figure 37: Influence of the miss-distances on the farfield noise. NACA-0012, $\hat{\Gamma} = -0.42$, M=0.73. (a) Acoustic pressure for different aerofoils at point P (50.0,0.0,-50.0) (b) Maximum BVI noise amplitude in terms of Sound Pressure Level for different miss-distances.

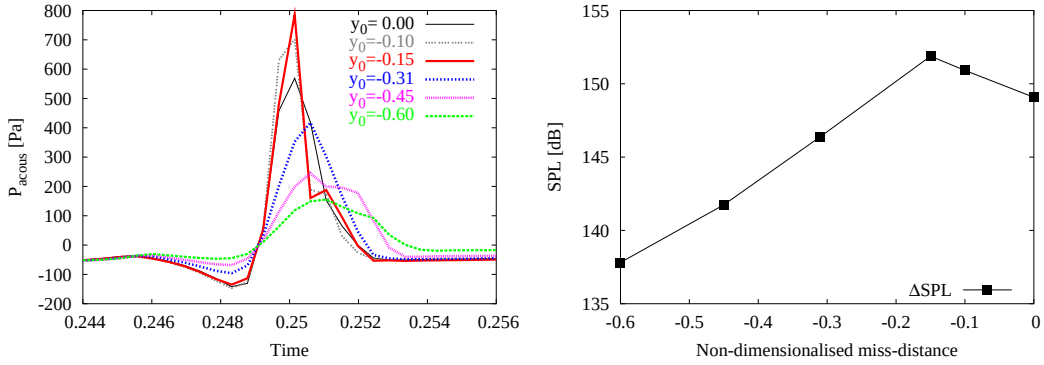

(a) (b)

Figure 38: Influence of the miss-distances on the farfield noise. NACA-0012, $\hat{\Gamma} = -1.8$, M=0.57. (a) Acoustic pressure for different aerofoils at point P (50.0,0.0,-50.0) (b) Maximum BVI noise amplitude in terms of Sound Pressure Level for different miss-distances.

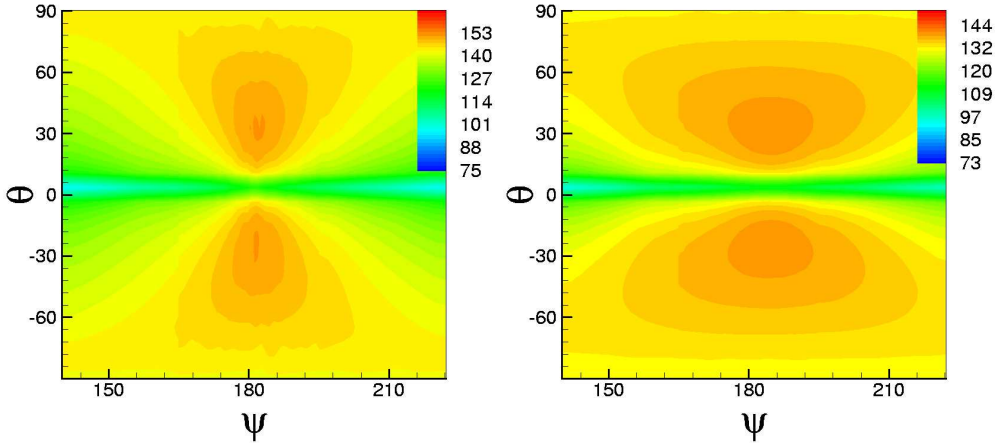

(a) OASPL in the (Ψ, θ) plane, $y_0 = 0.00$ (b) OASPL in the (Ψ, θ) plane, $y_0 = -0.60$

Figure 39: Contours of the OASPL for the range of azimuth angles Ψ where the BVI occurs. The elevation angle θ indicates the directivity patterns of the BVI noise below ($\theta < 0$) and above ($\theta > 0$) the helicopter. NACA-0012, (a) $y_0 = 0.00$, $\hat{\Gamma}$=-0.42, M=0.73 - (b) $y_0 = -0.60$, $\hat{\Gamma}$=-0.42, M=0.73.

Conclusions and Future work

A combination of CFD and CAA methods has been used for the study of the BVI problem. The potential of the method has been demonstrated for several flow cases suggesting that this technique is a valid, low-cost and easy to implement alternative to higher order CFD methods.

The obtained results highlight the importance of the aerofoil shape in the emitted sound during BVI and the complex relationship between the vortex characteristics and the resulting acoustic field. Of significant importance is the relationship between the radius of the vortex core and the intensity of BVI. The current set of results indicate that alleviation or even total control of the sound is possible provided the vortex core properties can be modified in an efficient way.

Further work needs to be carried out in three-dimensions in order to validate the proposed technique and clarify the role of vortex orientation in the emitted sound. In parallel, research in low dissipation and dispersion CFD algorithms is necessary which will allow the direct computation of the acoustic field without the need to apply aeroacoustics methods in the very near field of the CFD solution. Regarding the current acoustics module, further developments include modifications for ground reflection and turbulence.

Acknowledgements

This work was supported by Westland Helicopters Limited and the University of Glasgow.

References

[1] W.R Splettstoesser et al. The helinoise aeroacoustic rotor test in the DNW. Test documentation and representative results. Technical report, DLR-Mitt. 93-09, 1993.

[2] C. Kitaplioglu, F.X. Caradonna and C.L. Burley. Parallel blade-vortex interactions: an experimental study and comparison with computations. *Journal of the American Helicopter Society, pp. 272-281*, July 1997.

[3] J.C. Hardin and S.L. Lamkin. Concepts for reduction of blade/vortex interaction noise. *Journal of Aircraft Vol. 24, No. 2, pp. 120-125*, 1986.

[4] K.J. Badcock and B.E Richards. Implicit time-stepping methods for the Navier-Stokes equations. *AIAA. Vol. 34, No. 3, pp. 555-559*, 1996.

[5] J. Steinhoff and G.K. Raviprakash. Navier-Stokes computation of blade-vortex interaction using vorticity confinement. In 33^{rd} *Aerospace Sciences Meeting and Exhibit, Reno, NV*. AIAA 95-0161, January 1995.

[6] R. Lönher and C. Yang. Tracking vortices over large distances using vorticity confinement. *ECCOMAS CFD 2001, Swansea, Wales, Sept*, 2001.

[7] M. Murayama and K. Nakahashi and S. Obayashi. Numerical simulation of vortical flows using vorticity confinement coupled with unstructured grid. In 39^{th} *AIAA Aerospace Sciences Meeting & Exhibit, Reno, NV*. AIAA 2001-0606, January 2001.

[8] Y. Weren et al. Efficient Eulerian computation of realistic rotorcraft flows using vorticity confinement. In 39^{th} *AIAA Aerospace Sciences Meeting and Exhibit, Reno, NV*. AIAA 2001-0996, January 2001.

[9] R. Morvant, K.J Badcock, G.N Barakos and B.E. Richards. Aerofoil-vortex interaction simulation using the compressible vorticity confinement method, Friedrichshafen, Germany. In 29^{th} *European Rotorcraft Forum*, September 2003.

[10] J. Steinhoff et al. The computation of flow over helicopter rotors and complex bodies using vorticity confinement. Technical report, TN 37388, University of Space Institute, Tullahoma, USA, 2001.

[11] G. Hu and B. Grossman. Numerical method for vorticity confinement in compressible flow. *AIAA Journal, Vol. 40, No. 10, pp. 1945-1953*, October 2002.

[12] G. Hu. *The Development and Applications of a Numerical Method for Compressible Vorticity Confinement in Vortex-Dominant Flows*. PhD thesis, Viginia Polytechnic Institute and State University, Blacksburg, Virginia, June 2001.

[13] F. Farassat. Generalized functions and Kirchhoff formulas. In 2^{nd} *AIAA/CEAS Aeroacoustics Conference, State College, PA*. AIAA 96-1705, May 1996.

[14] F. Farassat. Theory of noise generation from moving bodies with an application to helicopter rotors. *NASA Technical Report*, December 1975.

[15] A.S. Lyrintzis and A.R. George. Farfield noise of transonic blade-vortex interaction. *Journal of American Helicopter Society - Vol. 34, No. 3, pp 30-39*, July 1989.

[16] A.S. Lyrintzis and E.K. Koutsavdis. Rotorcraft impulsive noise prediction using a rotating Kirchhoff formulation. *Journal of Airfraft, Vol. 33, No. 6, pp. 1054-1061*, Nov.-Dec. 1996.

[17] K.S. Brentner and F. Farassat. Modeling aerodynamically generated sound of helicopter rotors. *Progress in Aerospace Sciences 39, pp. 83-120*, 2003.

[18] F. Caradonna *et al.* Methods of the prediction of blade-vortex interaction noise. *Journal of the American Helicopter Society, pp. 303-317*, October 2000.

[19] R.K. Singh and J.D Baeder. Transonic effects on acoustics of blade-vortex interaction. *AIAA 200-1921*, June 2001.

[20] K.S. Brentner and F. Farassat. Helicopter noise prediction: The current status and future direction. *Journal of Sound and Vibration 170(1), pp. 79-96*, 1994.

[21] J.M. Gallman et al. Effect of wake structure on blade-vortex interaction. Phenomena: Acoustic prediction and validation. *Journal of Aircraft Vol 35, No. 2, pp. 267-273*, 1988.

[22] F. Farassat and G.P. Succi. The prediction of helicopter rotor discrete frequency noise. *Vertica Vol. 7, No. 4, pp. 309-320*, 1983.

[23] E. R. Booth Jr. Experimental observations of two-dimensional blade-vortex interaction. *AIAA Journal - Vol. 28, No. 8, pp. 1353-1359*, 1990.

[24] J.M. Gallman. Parametric computational study of isolated blade-vortex interaction noise. *AIAA Journal - Vol. 32, No. 2, pp. 232-238*, February 1994.

[25] S. Lewy and M. Caplot. Review of some theoretical and experimental studies on helicopter rotor noise. *Vertica Vol. 8, No. 4, pp. 309-321*, 1984.

[26] K.S. Brentner, C.L. Burley and M.A. Marcolini. Sensitivity of acoustic prediction to variation of input parameters. *Journal of the American Helicopter Society, pp. 43-52*, July 1994.

[27] B.W.-C Sim and F.H. Schmitz. Blade vortex interaction (bvi) noise: Retreating side characteristics, sensitivity to chordwise loading and unsteady aerodynamics. *Presented in the American Helicopter Society (AHS) Aeromechanics Specialists' Meeting, Atlanta, Georgia*, November 13-14 2000.

[28] A. Hassan et al. Effects of surface blowing/suction on the aerodynamics of helicopter rotor BVI - a numerical simulation. *Journal of the American Helicopter Society, pp. 182-194*, 1998.

[29] B.W.-C Sim, F.H. Schmitz and T. Aoyama. Near/far-field radiation of advancing side helicopter blade vortex interaction (bvi) noise. *Presented in the American Helicopter Society (AHS)* 56^{th} *Annual National Forum. Virginia Beach, Virginia*, May 2-4 2000.

[30] S. Lee and D. Bershader. Head-on parallel blade-vortex interaction. *AIAA Journal Vol. 32, No. 1, pp. 16-22*, 1994.

[31] H.-M. Lent et al. Mechanisms of transonic blade-vortex interaction noise. *Journal of Aircraft, Vol. 30, No. 1, Jan.-Feb.*, 1993.

[32] W.J. McCroskey and P.M. Goorjian. Interactions of airfoils with gusts and concentrated vortices in unsteady transonic flow. *AIAA paper 83-1691*, July 1983.

[33] W.J. McCroskey and G.R. Srinivasan. Unsteady interactions of transonic airfoils with gusts ans concentrated vortices. In *Advisory Group for Aerospace Research & Development, Neuilly sur Seine, France*. AGARD, 6-9 May 1985.

[34] J.C. Hardin and S.L. Lamkin. Aeroacoustic interaction of a distributed vortex with a lifting Joukowski airfoil. In *AIAA/NASA* 9^{th} *Aeroacoustics Conference, Willaimsburg, Virginia*. AIAA 84-2287, October 1984.

[35] E.R. Booth Jr. and J.C. Yu. Two-dimensional blade-vortex flow visualization investigation. *AIAA Journal - Vol. 24, No. 9, pp. 1468-1473*, September 1986.

[36] M.M. Rai. Navier-Stokes simulations of blade-vortex interaction using high-order accurate upwind schemes. In *AIAA* 25^{th} *Aerospace Sciences Meeting, Reno, NV*. AIAA 87-0543, January 1987.

[37] J.L. Ellzey and M.R. Henneke. The acoustic wave from a shock-vortex interaction: Comparison between theory and computation. *Fluid Dynamics Research 27, pp. 53-64*, 2000.

[38] S. Körber and J. Ballmann. Mechanisms and acoustics of blade-vortex-interactions. *Z. Flugwiss. Weltraumforsh. 19, pp. 397-406 - Springer-Verlag*, 1995.

[39] W.S. Kaminski and A.P. Szumowski. Acoustic effects of parallel vortex-airfoil interaction. *Journal of Sound and Vibration - Vol. 183, No. 2, pp. 209-220*, 1995.

[40] A.R. George and S.-B. Chang. Flow field and acoustics of two-dimensional transonic blade-vortex interactions. *AIAA paper - 84-2309*, 1984.

[41] A.S. Lyrintzis and Y. Xue. Noise mechanisms of transonic blade-vortex interaction. In *Presented at the AHS* 46^{th} *Annual Forum, Washington, DC*. American Helicopter Society, May 1990.

[42] J.S. Preisser, T.F. Brooks and R.M Martin. Recent studies of rotorcraft blade-vortex interaction. *Journal of Aircraft - Vol. 31, No. 5, pp. 1009-1015*, Sept.-Oct. 1994.

[43] B. Malovrh, F. Gandhi and L. Tauszig. Sensitivity of helicopter bvi-induced and vibration to variations in individual intraction-parameter. In 57^{th} *Annual Forum, Washington, DC*. American Helicopter Society, May 9-11 2001.

[44] F.X. Caradonna and C. Tung. Helicopter impulsive noise: Theoretical and experimental status. *Journal of Sound and Vibration, Vol. 109, No. 3, pp. 361-422*, 1986.